

Experimental investigation of SF<sub>6</sub>-O<sub>2</sub> plasma  
for the advancement of the anisotropic Si etch  
process

Khaled Alshaltami

May 2020

PhD

**Experimental investigation of SF<sub>6</sub>–O<sub>2</sub>  
plasma for the advancement of the  
anisotropic Si etch process**

*A thesis for the degree of*

**PHILOSOPHIÆ DOCTOR**

*presented to*

**DUBLIN CITY UNIVERSITY**

*by*

**Khaled Ali Essa Alshaltami, B.Sc., M.Sc.**

School of Electronic Engineering

Dublin City University

Research Supervisor:

**Prof. Stephen Daniels**

May 2020

## Declaration

I hereby certify that this material, which I now submit for assessment on the programme of study leading to the award of Doctor of Philosophy, Ph.D., is entirely my own work, that I have exercised reasonable care to ensure that the work is original, and does not to the best of my knowledge breach any law of copyright, and has not been taken from the work of others save and to the extent that such work has been cited and acknowledged within the text of my work.

Signed:  (Candidate)

ID No.: 12210331

Date: 17/05/2020



## Acknowledgement

After several intense years of research, today I am finally able to convey my thanks to everyone who contributed to this research work and supported it in one way or another. Though only my name appears on the cover of this thesis, many other people have significantly contributed to its production and I wish to acknowledge them here.

I am grateful to Prof. Stephen Daniels for giving me the opportunity to pursue my Ph.D. at Dublin City University. I would like to thank him and Prof. Conor Brennan for their support, encouragement and who were never too busy to give me their time when I needed advice.

I am also grateful for Prof. Dermot Barbizon's and Prof. Denis Dowling encouragement and valuable input. I would also like to thank Prof. Paul Swift for his knowledge of plasma physics and unconditional support provided to my research. Thanks also to all the team in the National Centre for Plasma Science and Technology (NCPST), the Electronic Engineering Department and the technical staff, especially Mr Conor Murphy, Mr Robert Clare and Mr Michael May. I would also like to extend my thanks to my colleagues (past and present) especially Jim Conway, Cezar Gaman, Muhammad, Guru, Sharath, Samir, Sean, Yang and Zhenning.

I gratefully acknowledge the financial support from the Ministry of Higher Education and Scientific Research of Libya.

Finally, I make special mention of my parents Rajah and Ali, who always motivated me to pursue higher studies, and also give my deep thanks to my wife Dr. Eman Mohamed, my daughters Mais, Mayar, Noor, Haneen and my family for their love, support and encouragement. <sup>24</sup>وَإِخْفِضْ لَهُمَا جَنَاحَ الذَّلِيلِ مِنَ الرَّحْمَةِ وَقُلْ رَبِّ ارْحَمْهُمَا كَمَا رَبَّيْتَنِي صَغِيرًا.

# Contents

List of figures.....	8
List of tables.....	11
List of publications.....	12
Abstract.....	13
Chapter 1 .....	18
1 Introduction .....	18
1.1 General overview of plasma.....	18
1.2 Plasma and its application in semiconductor industries.....	19
1.3 Surface engineering: Etching characteristics and variables .....	22
1.4 Role of plasma parameters in surface engineering .....	26
1.6 Chamber matching .....	29
1.7 Motivation.....	30
1.8 Thesis structure .....	34
Chapter 2 .....	36
Experimental setup and diagnostics techniques .....	36
2.1 Oxford Instruments PlasmaLab 80plus and PlasmaLab 100.....	37
2.2 Sample preparation and analysis .....	39
2.2.1 Photolithography.....	39
2.2.2 Scanning electron microscopy .....	48

2.3 Plasma diagnostic technique.....	50
2.3.1 Optical emission spectroscopy.....	50
2.3.2 Actinometry .....	51
2.3.3 Langmuir probe.....	54
Chapter 3 .....	58
Investigation of etch rate and etch profile variation due to additive oxygen and chamber geometry in SF <sub>6</sub> -O <sub>2</sub> plasma .....	58
3.1 Optical diagnostic of SF <sub>6</sub> -O <sub>2</sub> plasma.....	59
3.2 Study of etch rate .....	62
3.3 Study of etch profile.....	65
3.4 Study of atomic oxygen and fluorine concentrations in the plasma .....	68
3.5 Study of electron density.....	72
3.6 Comparison of etch rates between OIP 80+ and OIP 100 .....	74
3.7 Conclusion.....	76
Chapter 4 .....	78
Theoretical analysis of the ion energy distribution and relationship between etch rate and density in SF <sub>6</sub> -O <sub>2</sub> plasma .....	78
4.1 Theoretical analysis of ion energy distribution in RF plasma.....	78
4.2 Relationship between the etch rate and fluorine densities .....	82
Chapter 5 .....	86
Investigation of etching optimisation in capacitively coupled SF <sub>6</sub> -O <sub>2</sub> plasma ..	86
5.1 Ion energy distribution for RF plasma and its comparison with the experimental investigations.....	87
5.2 Experimental results and discussion .....	90
5.3 Summary .....	103

Chapter 6 .....	104
6.1 Summary, conclusions and recommendations for future research.....	104
6.2 Recommendations for future research .....	109
References .....	111

## List of figures

Figure 1.1: Schematics of (b) isotropic and (c) anisotropic etching .....	21
Figure 1.2: Anisotropy requirement for etching of a silicon wafer. The depth ( $d$ ) and lateral depth ( $\delta$ ) of the sidewalls were measured, and the ratio $\delta/d$ indicates their verticality.....	23
Figure 1.3: Simulation sidewall passivation.....	25
Figure 1.4: Densities, electric field and potential after formation of the sheath...29	29
Figure 2.1: Schematic of an RIE plasma chamber of PlasmaLab 80+, OIP 80+ 38	38
Figure 2.2: Schematic of an RIE plasma chamber of PlasmaLab 100, OIP 100 38	38
Figure 2.3: (a) The application of photoresist, (b) the excess resist is removed upon rotation, yielding a uniformed photoresist layer, (c) SEM image of the printed polymer layer .....	42
Figure 2.4: Soft-bake steps.....	43
Figure 2.5: Three possible UV exposure methods. (a) Contact printing (b) Proximity printing (c) Projection printing.....	45
Figure 2.6: Shows the steps after exposure when the mask design is encoded into the photoresist in the form of polymerised and unpolymerised resist and the development .....	46
Figure 2.7: Hard-bake steps .....	47
Figure 2.8: Shows the final step of photolithography. The sample was inspected under a microscope .....	47
Figure 2.9: Schematic of the SEM, Zeiss EVO LS-15 SEM system .....	49
Figure 2.10: Ideal I-V characteristic from a Langmuir probe. Real I-V characteristic curves typically do not have such easily identifiable features .....	55
Figure 3.1: Normalised EEDFs for plasmas with different oxygen concentrations as functions of the electron energy.....	61
Figure 3.2: Cross-sections of argon ( $\sigma^{750}$ ), fluorine ( $\sigma^{703}$ ) and oxygen ( $\sigma^{777}$ ) as functions of the electron energy .....	62

Figure 3.3: Silicon etch rate for the two chambers: OIP 80+ and OIP 100. The squares represent data for the OIP 80+ plasma source, and the circles represent data for the OIP 100 discharge.....	63
Figure 3.4: $\delta/d$ versus percentage of O <sub>2</sub> in the SF <sub>6</sub> -O <sub>2</sub> plasma of the plasma-etch reactors ( $d$ : depth of sidewall, $\delta$ : lateral depth of sidewall) .....	66
Figure 3.5: A typical SEM cross-section micrographs, (a) Etch profile obtained at 0 to 30% O <sub>2</sub> concentration for the OIP 80+, (b) Etch profile obtained at 0 to 30% O <sub>2</sub> concentration for the OIP 100.....	67
Figure 3.6: (a) Relative O atomic intensity ( $I_{777}/I_{750}$ ) and (b) relative F atomic intensity ( $I_{703}/I_{750}$ ) as a function of O <sub>2</sub> fraction measured in OIP 80+ and OIP 100 .....	69
Figure 3.7: Densities of (a) F atoms and (b) O atoms as functions of the O <sub>2</sub> fraction in SF <sub>6</sub> -O <sub>2</sub> in the plasma chambers. The squares represent data for the OIP 80+ chamber, and the circles represent data for the OIP 100 chamber.....	72
Figure 3.8: Electron density as a function of the O <sub>2</sub> fraction in SF <sub>6</sub> -O <sub>2</sub> in the plasma chambers. The squares represent data for the OIP 80+ chamber, and the circles represent data for the OIP 100 chamber .....	73
Figure 3.9: Ratio of etch rates between OIP 80+ and OIP 100 vs O <sub>2</sub> %.....	75
Figure 3.10: Ratio of densities between OIP 80+ and OIP 100 vs O <sub>2</sub> %.....	75
Figure 3.11: Etch rate vs fluorine density for OIP 80+ and OIP 100.....	76
Figure 4.1: Ion energy distribution, $f_i(E)$ , vs energy for different DC bias.....	80
Figure 4.2: Ion population vs ion energy .....	81
Figure 4.3: Locus of silicon etch rate ER and F atom density as the function of %O <sub>2</sub> in a SF <sub>6</sub> -O <sub>2</sub> plasma.....	83
Figure 4.4: Etch rate of Si versus F atom density. Arrows indicate the direction of increasing O <sub>2</sub> concentration in the feed [61].....	84
Figure 5.1: DC bias vs pressure .....	88
Figure 5.2: DC bias vs %O <sub>2</sub> .....	88
Figure 5.3: DC bias vs pressure for different %O <sub>2</sub> for peak etch rate .....	89
Figure 5.4: $f_i(E)$ vs energy for different pressure and %O <sub>2</sub> .....	90

Figure 5.5: Relative intensity of the F atom as a function of %O <sub>2</sub> in SF <sub>6</sub> -O <sub>2</sub> ....	91
Figure 5.6: Values of fluorine densities as a function of %O <sub>2</sub> at different pressures .....	92
Figure 5.7: The density of F atoms as a function of power at different O <sub>2</sub> concentrations in 200 mTorr .....	93
Figure 5.8: The density of O atoms as a function of power at different O <sub>2</sub> concentration and 200 mTorr .....	94
Figure 5.9: Etch rate as a function of %O <sub>2</sub> for different pressures .....	94
Figure 5.10: Electron density as a function of the fraction of O <sub>2</sub> corresponding to the pressure values observed in the SF <sub>6</sub> -O <sub>2</sub> plasma system .....	96
Figure 5.11: Peak of the etch rate as a function of pressures for different oxygen concentrations .....	97
Figure 5.12: Values of $\delta/d$ for each profile as a function of the fraction of oxygen in SF <sub>6</sub> -O <sub>2</sub> discharge .....	98
Figure 5.13. Etch profile obtained at 100 mTorr and 25% oxygen concentration, where ( $d$ ) is the depth and ( $\delta$ ) is the lateral depth.....	100
Figure 5.14: Ion population vs ion energy.....	102

## Nomenclature

RF	radio frequency
DC	Direct current
$T_e$	electron temperature
$T_i$	ion temperature
$T_g$	gas Temperature
PVD	physical vapor deposition
CCP	capacitively coupled plasma
SEM	scanning electron microscope
$ER$	etch rate
$d$	depth
$\delta$	lateral depth
$\Gamma_{i,e}$	the flux of electrons and ions
$n$	density
$\langle v \rangle$	average velocity
IEDF	ion energy distribution function
$-V_c$	negative self-bias
$V_{pp}$	plasma potential
$V_{dc}$	DC bias
$k_B$	Boltzmann constant
OIP 80+	oxford instrument plasmalab 80+
OIP 100	oxford instrument plasmalab 100

sccm	standard cube centimeter per minute
rpm	revolutions per minute
UV	ultraviolet
DCU	Dublin City University
OES	optical emission spectroscopy
IC	integrated circuit
F	Fluorine
O	Oxygen
$n_F$	Fluorene density
$n_O$	Oxygen density
$n_{Ar}$	Argon density
$n_e$	electron density
$k_x$	electron impact excitation rate constant
$I_F$	Fluorine density
$I_O$	Oxygen density
$I_{Ar}$	Argon density
$\varepsilon$	electron energy
$\sigma^x(\varepsilon)$	electron impact excitation cross section
$f(\varepsilon)$	electron energy distribution
$P$	pressure
$V_f$	floating potential
$I_e$	electron current

$I_i$	ion current
$\sigma^{750}$	Argon cross section
$\sigma^{703}$	Fluorine cross section
$\sigma^{777}$	Argon cross section
EEDF	electron energy distribution function
IED	ion energy distribution
$E$	ion energy
$\tau_{ion}$	ion transit time through sheath
$\tau_{rf}$	time period of the RF cycle
$f_i(E)$	ion energy distribution function
$IP$	ion population
$E_{act}$	activity energy
$S$	sheath thickness
$e$	electron charge
$\epsilon_0$	vacuum permittivity

## **List of tables**

Table 2.1: Main differences between two chambers.....	39
Table 2.2: The major steps involved within photolithography: (a) Wafer cleaning (b) Spin coating (c) Soft-baking (d) UV exposure (e) Development (f) Hard-baking (g) Inspection.....	40
Table 3.1: List of probable chemical reactions in the CCP dry etch system.....	64

## List of publications

**Alshaltami, Khaled A.**, Muhammad Morshed, Cezar Gaman, Jim Conway, and Stephen Daniels. "Experimental investigation of SF<sub>6</sub>-O<sub>2</sub> plasma for advancement of the anisotropic Si etch process." *Journal of Vacuum Science & Technology A: Vacuum, Surfaces, and Films* **35**, no. 3 (2017): 031307.

**Alshaltami, Khaled A.**, and Stephen Daniels. "Investigation of etching optimization in capacitively coupled SF<sub>6</sub>-O<sub>2</sub> plasma." *AIP Advances* **9**, no. 3 (2019): 035047.

### List of main conferences / Seminars attended

Short Course on "Compound Semiconductor Device Fabrication", in Tyndall National Institute, Cork, Ireland from February 8th to February 12th, 2016.

Talk given at National Centre for Plasma Science & Technology (NCPST) group, Dublin City University in 2016. Title: Experimental Investigation of SF<sub>6</sub>-O<sub>2</sub> Plasma for the Advancement of Silicon Etch Process.

Poster presented on The Plasma Nanoscience Conference was held in The Helix, DCU. From 19th-20th March 2014. Title: Design and Control of Plasma Surface Engineering Processes.

Poster presented on Libya Higher Education Forum. A Vision for the Future 5 – 6 June 2014, London. [www.libyaed.com](http://www.libyaed.com).

Poster presented on Intel Ireland Research Conference, Clontarf Castle, Dublin, 21- 22 November 2013, page number 65. Title: Effect of O<sub>2</sub> Addition for Si Etch Process in SF<sub>6</sub>-O<sub>2</sub> Discharge.

## **Abstract**

Khaled Alshaltami

Experimental investigation of SF<sub>6</sub>-O<sub>2</sub> plasma for the advancement of the anisotropic Si etch process

In semiconductor production, the wafers should be processed in different chambers which are readily available, rather than waiting for the right chamber. To avoid these time delays, and the associated cost, chamber matching is generally carried out. This study examines the impact of varying the concentrations of oxygen/fluorine and the operating pressure in an SF<sub>6</sub>-O<sub>2</sub> plasma in two capacitively coupled plasma etch chambers with different geometries. Silicon wafers were used to investigate the anisotropic nature of the etch profiles. The oxygen and fluorine concentrations were measured via optical emission spectroscopy using the actinometry technique, which requires the electron energy distribution function to remain unchanged under the different plasma conditions employed in this work. A Langmuir probe was used to investigate the electron energy distribution function where the chamber pressure, power and process duration were kept constant, and the oxygen concentration was varied from 0 to 60%. The results showed that in both chambers the atomic concentrations of fluorine increased rapidly when the percentage of oxygen in the SF<sub>6</sub> plasma was increased to 20%, and decreased with further addition of oxygen at

10 mTorr/200 W. However, the peak of fluorine density occurred at a higher oxygen percentage (>20%) when the operating pressure was increased to 600 mTorr. Scanning electron microscopy showed an etch feature with a minimal lateral depth at various oxygen concentrations in both chambers. A qualitative theoretical analysis of the ion energy distribution and its correlation with the etch rate and the density of F in SF<sub>6</sub>-O<sub>2</sub> plasma is also presented. In conclusion, chamber matching can be achieved through the experimental investigations carried out in this study, focusing on chamber geometry, fluorine/oxygen concentrations and operating pressure to achieve optimal etch rates and profile.

# Chapter 1

## 1 Introduction

### 1.1 General overview of plasma

#### *1.1.1 What is the plasma state?*

Plasma is defined as the fourth state of matter after solid, liquid and gas. Plasma was first defined by Crookes in the late nineteenth century [1], based on his studies on understanding the behaviour of gas in an empty glass tube. Plasma is generally characterised in terms of its temperature and pressure. For example, in low temperature plasmas, electron temperature ( $T_e$ )  $\gg$  ion temperature ( $T_i$ )  $\sim$  gas temperature ( $T_g$ ). Other types of plasmas are called equilibrium plasma in which  $T_e \sim T_i$ . These are mainly used for high temperature applications, such as fusion plasma [3]. On the other hand, high pressure plasmas are widely used for biomedical applications. We have already seen many applications of low pressure plasma in semiconductor industries, such as faster computer processors, plasma displays, photovoltaic cells, material fabrication, plasma cleaning, plasma etching and plasma deposition [2], [3]. This is achieved through low temperature (also called cold) low pressure plasmas.

### *1.1.2 Plasma in a laboratory*

Cold plasmas can be generated in an evacuated chamber by means of a radiofrequency or DC electric field applied to electrodes. Electrons are accelerated in the electric field and can transfer energy to the neutral gas atoms through collisions. Depending on the amount of the transferred energy, various reactions such as excitation, dissociation and ionisation may occur.

### *1.1.3 Plasma processing*

Plasma involves mainly two types of interaction: interactions between the plasma generated species, and interaction between the plasma species and surrounding surfaces. The surrounding surfaces can be a chamber wall, electrodes, probes, or any material surface which needs to be modified. These interactions are mainly governed by the electrons since the electrons are mainly responsible for various kinematics and emission. All fundamental plasma parameters, such as Debye length, plasma frequency and conductivity, are also dependent on the electron density [4].

## **1.2 Plasma and its application in semiconductor industries**

Semiconductor device fabrication progressed from a 10 micrometer integrated chip to nanometer-sized in few decades (10 nanometer in 2017) [5]. This trend

follows Moore's law which is the observation that the number of transistors in a dense integrated circuit doubles approximately every two years. There are many processes involved in the fabrication of chips, such as **deposition, removal, patterning,** and **modification.** Deposition includes coating or transfer of material to the wafer using techniques like PVD (physical vapor deposition). Removal involves removing material from the wafer using etch processes (either wet or dry). Patterning, generally referred to as lithography, shapes the deposited materials. Modification involves doping processes through ion implantation.

Dry removal, also called **plasma etching,** is an integral part of semiconductor fabrication in the microelectronics industry, as it enables nano-electronic fabrication. This method refers to any process where plasma is used to etch the surface of an object, removing material from areas identified by the lithography process. It is also required to create structures for functional use and to remove oxide layers below features to allow for motion. Dry plasma etching has many benefits over wet etching, which employs chemical or liquid etchants, as it improves the physical properties of etched material, has a high etch rate, removes unwanted organic material from the surface, is less risky and has volatile by-products.

### *1.2.1 Types of plasma etching: Anisotropic etching and isotropic etching*

There are two types of plasma etching: Anisotropic etching and isotropic etching, as shown in figure 1.1.

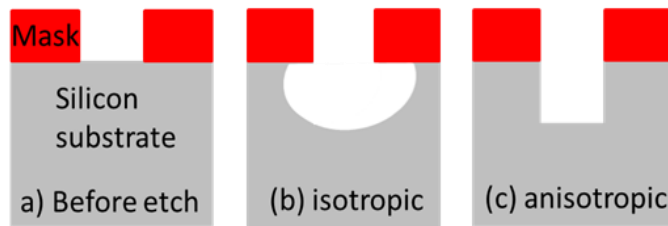


Figure 1.1: Schematics of (b) isotropic and (c) anisotropic etching

Both isotropic and anisotropic etching are different in terms of their profile shape, as shown in figure 1.1. In the case of anisotropic etching, plasma etches the substrate only along the vertical depth, whereas in the case of isotropic etching, plasma etching takes place uniformly in all directions.

### *1.2.2 How does plasma etching takes place?*

Anisotropic etching and isotropic etching may be accomplished using capacitively coupled plasma (CCP) low-pressure plasma systems. The plasma system consists of two symmetrical electrodes and a ground electrode on which the sample to be etched is placed. The system is then filled with an etchant gas ( $\text{CF}_4$ ,  $\text{SF}_6$ ,  $\text{O}_2$  or  $\text{Cl}$ , for example) and electrodes are driven by a radiofrequency source (RF driven at

13.56 MHz) to create a highly reactive plasma. The surface engineering will depend on the type of gas used, the nature of the sample to be etched and the type of etching required.

In plasma, both radicals and ions play an important role in etching. However, radicals are chemically active, and they react at the surface of the substrate, producing volatile products. On the contrary, the role of ions is to perform physical bombardment of the surface, causing etching. The differences in the population of radicals and ions determine the dominant processes in the plasma etching, such as sputtering, pure chemical etching and ion etching [6].

## **1.3 Surface engineering: Etching characteristics and variables**

### *1.3.1 Define the etch rate*

The etch rate is determined by the volume of material removed per unit time. In practice, the etch is carried along the full length of the substrate. Thus, the cross-section etch is sufficient to determine the etch rate. The maximum depth achieved irrespective of shape per unit time is defined as the etch rate. Etch rate = depth/time. A scanning electron microscope (SEM) taken at a sufficient resolution was used to analyse the processed sample's surface by measuring the depth of the Si etch profile.

### 1.3.2 Anisotropy etch profile

The anisotropy in the etch profile is characterised using the parameter lateral etch ratio (horizontal over vertical etch rate). For example, the ratio equal to one corresponds to isotropic etching.

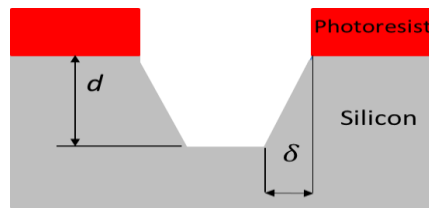


Figure 1.2: Anisotropy requirement for etching of a silicon wafer. The depth ( $d$ ) and lateral depth ( $\delta$ ) of the sidewalls were measured, and the ratio  $\delta/d$  indicates their verticality

The anisotropy of the etching process can be studied by measuring the depth ( $d$ ) and lateral depth ( $\delta$ ) of the sidewalls in the Si etch profile (see figure 1.2). The ideal anisotropy is when the  $\delta/d = 0$ . Both  $d$  and  $\delta$  are obtained to estimate the etch rate ( $d/\text{time}$ ) and lateral etch ratio ( $\delta/d$ ) as a function of oxygen concentration in the  $\text{SF}_6\text{-O}_2$  discharge. Etch uniformity is a measure of process repeatability within the wafer and wafer to wafer. The selectivity is the ratio of etch rates of different materials [7].

### *1.3.3 Role of various gases governing the processing plasmas*

Because of the different chemical composition and properties of the gases used in plasma etching, the surface characteristics of the substrate can be altered. Therefore, these gases have their own importance and these are briefly explained here [7].

1.  $\text{CCl}_4$ ,  $\text{SF}_6$  and  $\text{CF}_4$ : **Saturates**

The saturates are chemically not very reactive, but dissociate into reactive species through electron collisions.

2.  $\text{CCl}_3$ ,  $\text{SF}_5$ ,  $\text{CF}_3$ : **Unsaturates**

These gases mostly react with the substrate.

3. O,  $\text{O}_2$  and  $\text{O}_3$ : **Oxidants**

These gases react with the unsaturates and convert them into volatile products or etchants.

4. F, Cl and Br: **Etchants**

These species are very reactive and mainly contributes towards the etching of the surfaces.

5. Ar, He and  $\text{N}_2$ : **Non-reactive gases**

These gases are used in very tiny quantities to diagnose the plasma, such as for actinometry.

### 1.3.4 Chemistry of fluorine-based etching and oxygen-based surface passivation in SF<sub>6</sub> plasma

Fluorine works as an etchant in the plasma and is responsible for the vertical depth. The ion flux and energy govern the etching process. However, in order to achieve an anisotropic etch profile, the dominance of the fluorine has to be suppressed. This is achieved through the surface sidewall passivation technique with the addition of O<sub>2</sub> to SF<sub>6</sub> plasma [8], [9].

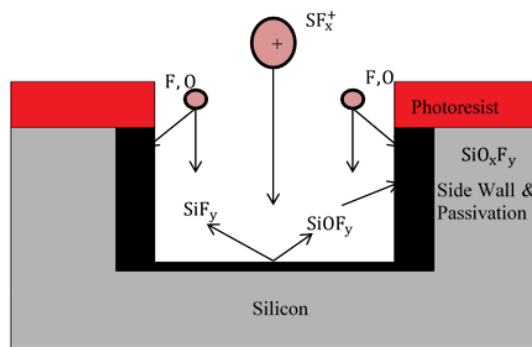


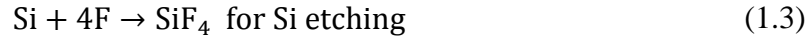
Figure 1.3: Simulation sidewall passivation

This chemical recipe produces a silicon oxyfluoride (SiO<sub>x</sub>F<sub>y</sub>) film through the following chemical reactions.

Dissociation reactions:



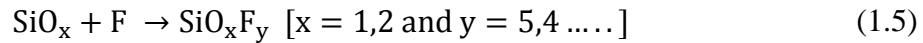
Surface reaction:



Surface oxidation:



Combination:



$\text{SF}_6$  produces F radicals for the chemical etching of silicon forming volatile products such as  $\text{SiF}_x$  which are easily removed from the surface.  $\text{SF}_6$  is the source of  $\text{SF}_x^+$  ions which are responsible for removal of the siliconoxyfluoride  $\text{SiO}_x\text{F}_y$  layer at the trench bottom, forming the volatile product sulphuroxyfluoride  $\text{SO}_x\text{F}_y$  and allowing silicon etching to proceed further [8].

## **1.4 Role of plasma parameters in surface engineering**

Diagnostics of basic plasma parameters are very important to understand the plasma etching processes and to achieve a desired anisotropic etch profile. In this section, we have discussed some of these parameters and their relevance in processing plasmas.

### *1.4.1 Ion flux*

According to the kinetic theory, the flux of electrons and ions with a random velocity distribution is given by

$$\Gamma_{i,e} = n_{i,e} \langle v_{i,e} \rangle \quad (1.6)$$

where  $n$  is the density and  $\langle v \rangle$  is the average velocity. Because of the lighter mass of electrons, their flux is larger as compare to the ions. The whole etching process depend on how the ion flux interacts with the solid surfaces. For example, low ion energy reduces the physical damage to the wafer surface, improves the selectivity of the process, enhances the etch rate and results in improved anisotropy.

These positive ions are mainly accelerated through plasma sheath potential (a few hundred volts) adjacent to the electrodes. The whole ion flux is represented by the ion energy distribution function (IEDF). The IEDF varies with the RF power and pressure. For example, by increasing the RF power, one can increase the ion density. On the other hand, electrodes' size or the ratio of their sizes can also influence the ion energy [10]. Any variation in the ion flux or energy can alter the plasma etching processes.

### *1.4.2 Plasma potential and DC bias in CCP-RF discharges*

Plasma potential is the average potential in a space between the charged particles. It is important to note that the plasma potential adjusts itself to a value in order to

maintain quasi-neutrality. In CCP-RF discharges, the plasma is mainly sustained by the alternating current which traverses the sheath between electrodes and plasma. The addition of negative self-bias ( $-V_c$ ) and plasma potential ( $V_{pp}$ ) gives us the DC bias ( $V_{dc}$ ) in the plasma ( $V_{dc} = -V_c + V_{pp}$ ). This  $V_c$  voltage accelerates the ions towards the powered electrode and can vary depending on the pressure and power of the plasma. The plasma potential can be measured using a Langmuir probe. However, the exact value of  $V_{pp}$  requires dedicated analysis of current-voltage characteristics, as the sheath voltage can affect the accuracy of the probe results [11]. The diagram below shows the schematic of the plasma and various potentials governing the plasma.

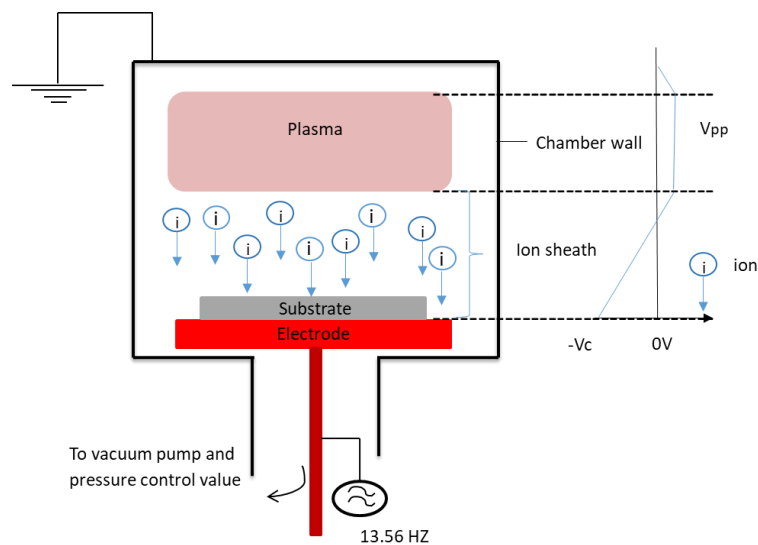


Figure 1.4: Densities, electric field and potential after formation of the sheath

### *1.4.3 Electron energy (electron temperature)*

Plasma is in a thermal equilibrium state, which means internal energy is uniformly allocated to all the plasma species. This can be quantified by a parameter called electron temperature. In the RF electric field, only the charged particles present in the plasma respond to the field and gain kinetic energy. Neutrals exchange this energy from the charged particle through the collisional process. The average energy can be defined as  $1.5k_B T_i$ , where  $k_B$  is the Boltzmann constant. Charged ions convert into fast-moving neutrals through the charge exchange process, whereas electrons, due to their smaller mass, compared to the neutrals transfer less energy to the neutrals. Because of this reason, ions and neutrals are nearly at the same temperature, whereas electrons are comparatively hot. Due to this fact, the low-pressure plasmas are called cold plasma.

## **1.5 Chamber matching**

In semiconductor production, the wafers are to be processed in different chamber which is readily available rather than waiting for the right chamber. To avoid these delays, generally chamber matching is carried out. Chamber matching is where the performance of the chamber being setup is compared to data from a set of known good chambers. One previous method of chamber matching has been to obtain performance data from the chambers in question and compare it to some performance specification. While historically the primary approach of acquiring

data for chamber matching has been to use on-wafer performance (i.e., etch rates, uniformity, etc.). More recently, due to the large amounts of data provided by newer systems, there has been a change of approach to detect chamber differences directly without checking for on-wafer performance [12]. Eliminating the need to check for on-wafer performance saves both time and cost appreciably. The chamber can be operated using methods to monitor and control the process. However, with such methods, the manufacturing process becomes more sophisticated and expensive [13]. Most of the methods are based on learning algorithms, thus ignoring the knowledge of chamber dimensions.

With the advent of technological evolution, chamber design has undergone a sea change to deliver high density plasma for better etching. In addition, incorporation of probes and sensors for in situ measurement and health checks constrict the effective utilisation of chambers. Thus, introduction of a newer generation of chambers may ironically delay the speed of bulk processing and decrease productivity. Therefore, a need exists for a method, or methods, to provide a more accurate way of chamber matching.

## **1.6 Motivation**

In the microelectronics sector, plasma etching is often used to modify the physical and chemical properties of metals including oxides, nitrides etc. Plasma etching was first investigated by the group of Agostino *et al.* in 1980s. [14] In this

research work, they have identified that the etching species in the plasma compete with oxygen atoms on the Silicon surface for chemisorption. The same group presented the use of actinometry technique in optical diagnostics of plasma etching mixtures of SF<sub>6</sub>-O<sub>2</sub>. In 1988, Tachi *et al.* [15] presented a new low temperature reactive ion etching carried by SF<sub>6</sub> plasma. Later in 1995, Legtenberg *et al.* [16] investigated the etching properties as a function of materials used for cathode and mask. In 1995, Jansen *et al.* [17] provided the detailed survey of results related to the etching material of interests in micromechanics and explain that plasma etching is extremely sensitive to many variables, making etch results inconsistent and irreproducible.

Reactive Ion Etching (RIE) has two main advantages in semiconductor industries i.e. high etching rate and anisotropic etching as demonstrated by Nojiri K. *et al.* (1996) [18] and Jansen H. *et al.* (1996) [19]. The anisotropic etching profile can be achieved by physical sputtering and chemical reaction of reactive species with the Silicon [Mansano RD. *et al.* (1999) [20] and Yunkin VA. *et al.* (1994) [21].

It is important to achieve control over the Fluorine density and DC Bias voltage in order to influence the etching profile and etch rate. This can be done by varying RF power, gas flow rate, ratios of SF<sub>6</sub> to O<sub>2</sub> gas flow rate and the chamber pressure Jansen H. *et al.* (1996) [19].

In 1997, Chen *et al.* [22] performed a numerical computational study on the ion sheath collisions and how it affects the etch profile. The increase in operating pressure results in significant number of collisions and makes the etch profiles more rounded and less rectangular. The lower pressure of 10 mTorr also has the potential to affect the shape of the etch profile. In 2004, Gomez *et al.* investigated the effect of pressure on etch characteristics and revealed that etch rate decreases rapidly beyond 20 mTorr and etch profiles become rectangular. The etch rate also increases with an increase in RF DC bias [23] and later in 2011 discovered that etch rate increases with RF power [24].

In 2004, Zou *et al.* [25] further understood the effect of oxygen concentration on both etch rate and etch profile over a wide range of pressures. Zou concluded that the etch rate and etch profile can be controlled by controlling the O<sub>2</sub> concentration and pressures. However, the research requires more detailed investigation to understand the optimum conditions for the anisotropic etch profile. In 2008, Lim *et al.* [26] studied the roles of F and O radicals in the formation of via structures and its effect on the vertical etching rates. In 2012, Morshed *et al.* [27] studied the electron density and fluorine density as a function of percentage of oxygen in an SF<sub>6</sub>-O<sub>2</sub> plasma. However, the detailed study on etch process and how it changes with the plasma parameters has not been investigate in this research. The etch profile is greatly affected by strong passivation on sidewall especially when there is a higher percentage of O<sub>2</sub> is

pumped into the plasma Donnelly V. M. *et al.* (2013) [28] and Kim B. *et al.* 2013 [29].

In semiconductor production, the wafers are to be processed in different chambers which is readily available rather than waiting for the right chamber. To avoid these time delays and associated cost, generally chamber matching is carried out. However, the control of anisotropic etching profile using different RIE system is key research challenge Pankajakshan P. *et al.* (2017) [30]. In addition, the knowledge of various operating parameters such as concentration of Oxygen and Fluorine, pressure, power and their impact on the etching process is crucial. Another important consideration is how the relative concentrations of species are substrate dependent Stuckert E. P. *et al.* (2017) [31]. Yang, Dongxun *et al.* (2019) [32] investigated the vertical sidewall trench etching on silicon substrate and modelled etching using artificial neural network.

The motivation of this PhD work is to demonstrate the optimum etch conditions over a broad range of operating parameters such as power, pressure, gas flows, and bias voltage. In addition, the etch profile and etch rates has been compared between two geometrically different chamber. The research gives a broader perspective of the chemical reactions and parameter selection to achieve desired etch conditions in the SF<sub>6</sub> plasma.

## 1.7 Thesis structure

Chapter 1: In the first chapter, we discuss the motivation behind this research work. This also includes fundamentals of the plasma, its parameters and plasma etching.

Chapter 2: This chapter covers the description of the CCP plasma systems (OIP 80+ and OIP 100) that are used to study the SF<sub>6</sub>-O<sub>2</sub> plasma. In addition, a description of the plasma diagnostic techniques and surface characterisation techniques related to the research work are presented.

Chapter 3: This chapter presents a comparative study of SF<sub>6</sub>-O<sub>2</sub> plasma in both CCP chambers which investigates etch rate and etch profile variation due to additive oxygen and chamber geometry in SF<sub>6</sub>-O<sub>2</sub> plasma.

Chapter 4: This chapter describes theoretical analysis of the ion energy distribution and discusses the relationship between etch rate and density of F in SF<sub>6</sub>-O<sub>2</sub> plasma.

Chapter 5: This chapter is an extension of the research work carried out in chapter 3. This includes the study of the peak etch rate and etch profile as a function of system pressure and power.

Chapter 6: This chapter summarises the research work outcomes as well as providing the scope of the research work following on from it that is to be carried out in future.

## **Chapter 2**

# **Experimental setup and diagnostics techniques**

This chapter describes the experimental setup used for the plasma processing study of Si using the SF<sub>6</sub>-O<sub>2</sub> plasma. A detailed description of the various plasma diagnostic techniques used and methods to understand the plasma etching process are also elaborated.

## **2.1 Oxford Instruments PlasmaLab 80plus and PlasmaLab 100**

Two capacitively coupled plasma chambers have been used to study the SF<sub>6</sub>-O<sub>2</sub> plasma etch processes. Both chambers belong to commercial plasma systems manufactured by Oxford Instruments (United Kingdom), referred as OIP 80+ and OIP 100. The schematics of the chambers are shown in figure 2.1 and 2.2.

Figure 2.1 shows the schematic of plasma chamber OIP 80+ fitted with vacuum pumps, two parallel stainless-steel electrodes and a radiofrequency (RF) (13.56 MHz) power supply. The electrodes are separated by a 46 mm distance. The bottom electrode is powered by an RF source and has a diameter of 240 mm. Figure 2.2 shows the schematic of plasma chamber OIP 100. This is similar to OIP 80+ except that the separation between the electrodes is 53 mm. The RF electrode has a diameter of 300 mm, and both electrodes are made of stainless steel. The ratio of the total cylindrical volume of OIP 80+ to that of OIP 100 was calculated to be approximately 1:2.16. The silicon wafers were loaded manually in OIP 80+, while a built-in load lock system in OIP 100 allowed the sample to be loaded without venting the chamber.

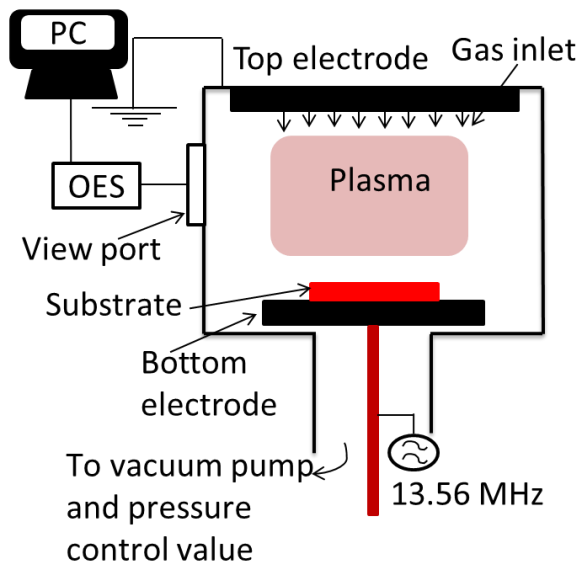


Figure 2.1: Schematic of an RIE plasma chamber of PlasmaLab 80+, OIP 80+

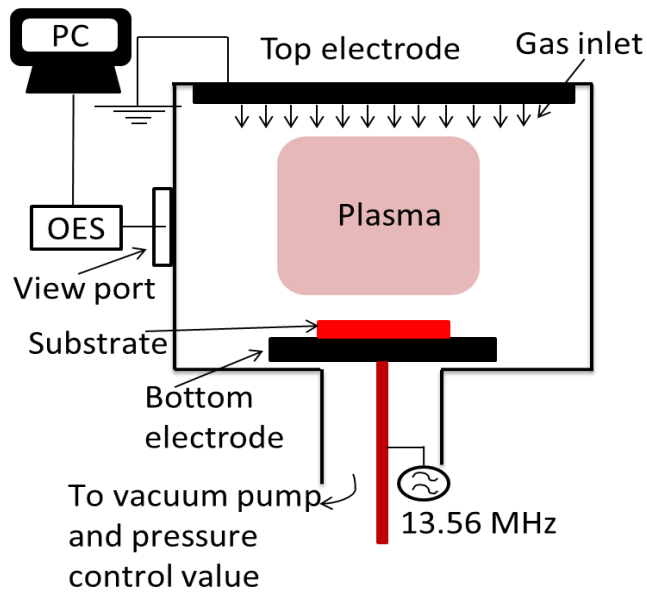


Figure 2.2: Schematic of an RIE plasma chamber of PlasmaLab 100, OIP 100

Both OIP 80+ and OIP 100 have been used to etch the silicon substrates and to investigate the  $\text{SF}_6\text{-O}_2$  plasma discharge. A capacitively coupled plasma is

generated by a 13.56 MHz RF power source. The silicon wafers were used; they had a specific pattern produced by a positive photoresist via photolithography. The RF power, pressure, gas-flow rate and process duration for both chambers were kept constant at 200 W, 10 mTorr, 50 sccm and 5 min, respectively. The oxygen fraction in the SF<sub>6</sub>-O<sub>2</sub> plasma was varied from 0 to 60 %.

Table 2.1: Main differences between two chambers

	PlasmaLab 80+	PlasmaLab 100
Ground electrode size	24 cm diameter	30 cm diameter
Bottom electrode size	200 mm	200 mm
Ratio of electrode size	1.2	1.5
The ratio of the total cylindrical volume of OIP 80+ to that of OIP 100 was calculated to be approximately 1:2.16.		

## 2.2 Sample preparation and analysis

### 2.2.1 Photolithography

Photolithography is the process of transferring geometric shapes from a mask to the surface of a prepared substrate. Photolithography involves several steps, which are summarised by the illustrations and flow chart of table 2.2.

(a)	Wafer cleaning
(b)	Spin coating
(c)	Soft-baking
(d)	UV exposure
(e)	Developer
(f)	Hard-back
(g)	Inspection

Table 2.2: The major steps involved within photolithography: (a) Wafer cleaning (b) Spin coating (c) Soft-baking (d) UV exposure (e) Development (f) Hard-baking (g) Inspection

#### 2.2.1.1 Wafer cleaning

The substrates are stripped of organic and inorganic surface contaminants to guarantee strong adhesion. The wafers that were used for this study were new and used for the first time. The silicon wafers were cut into pieces of approximately 2.5 cm × 2.5 cm. The pieces were then cleaned by blowing clean dry air to get rid of the silicon particles sticking on the pieces to achieve better adhesion between the substrate and the photoresist on the wafer.

### 2.2.1.2 Spin coating

The photoresist is a light-sensitive organic polymer which is subdivided into two groups – positive and negative – based on its action. Positive photoresist exposed to electromagnetic radiation becomes more sensitive to chemical etching than the unexposed area. On the other hand, the negative resist area becomes chemical resistant. As higher resolution can be achieved with positive photoresists, it is the preferred choice with micro-fabrication processes. The positive photoresist of S1818 is used in this work.

Spin coating is the principal mechanism for the application of photoresist films upon planar substrates. In figure 2.3(a), the substrate is mounted on a vacuum chuck and the resist is dispensed into the wafers' centre. The S1818 photoresist was applied and spun at 3,000 rpm for 40 seconds, forcing the excess resist to the substrate perimeter where it builds up prior to its ejection. The centrifugal forces caused by the rotation enable the distribution of a uniform coating, as shown in figure 2.3(b). The distribution of an unformed film is critical in ensuring the reproducibility of development times and resolution. The thickness of the resist,  $H$  is a function of the rotational speed and the polymers concentration and molecular weight of the polymer. An empirical expression for  $H$  is given by:  $H=AC\eta/\omega$  Where  $A$  is the calibration constant,  $C$  is the polymer concentration in a gram per liter,  $\eta$  is the intrinsic viscosity of photoresist and  $\omega$  is the rotation per

minutes [33]. In this work, the thickness of the photoresist deposited on the silicon wafer is  $2.3\ \mu\text{m}$ , measured by SEM.

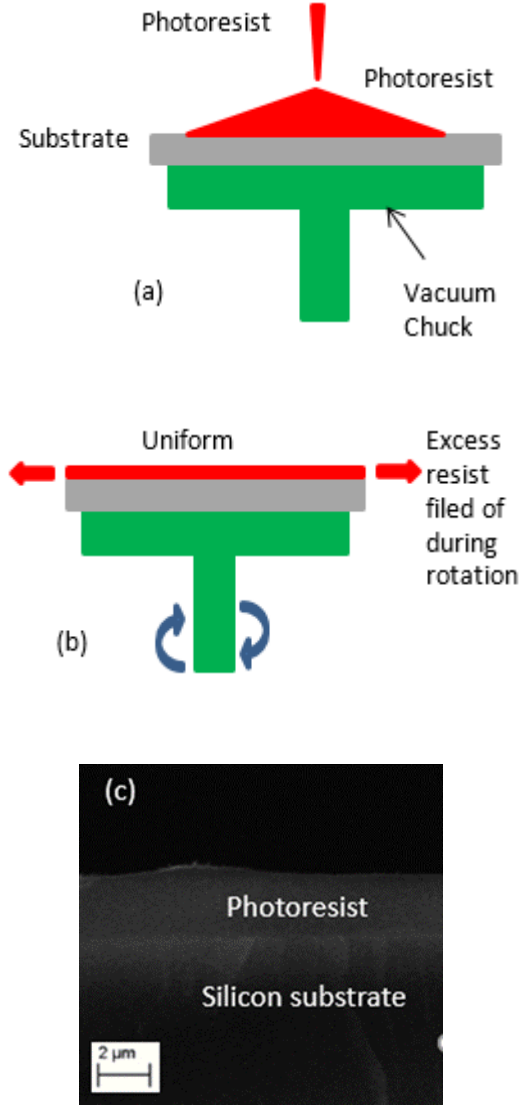


Figure 2.3: (a) The application of photoresist, (b) the excess resist is removed upon rotation, yielding a uniform photoresist layer, (c) an image of the printed polymer layer

### 2.2.1.3 Soft-baking

After spin coating, the resist still has a large solvent content. The wafer is placed on a hot plate and soft-baked to the temperature of 60°C for 30 seconds as shown in figure 2.4. The excess solvent is evaporated in a controlled manner and adherence between the resist and substrate is increased. It is only after soft-baking that the resist becomes photosensitive. The soft-baking temperature and the amount of time the wafer is heated are critical parameters, as over-baking results in the degradation of resist photosensitivity, while under-baking leads to excess coating solvent.

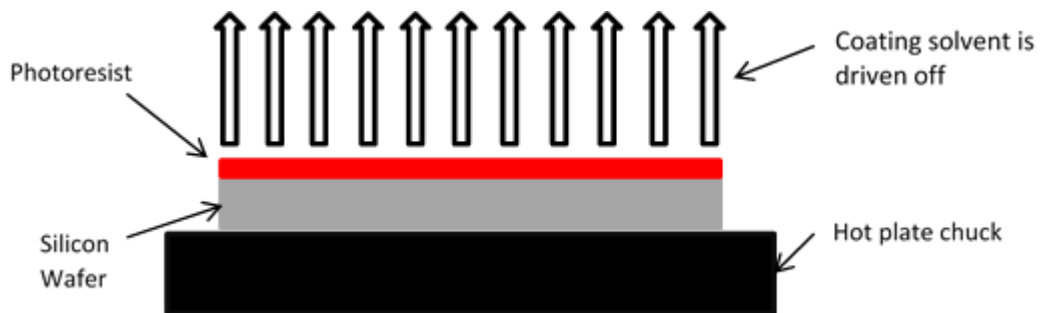


Figure 2.4: Soft-bake steps

### 2.2.1.4 UV exposure

There are three possible UV exposure methods: Contact printing, proximity printing and projection printing. The micro-fabrication cleanroom (class 100 and 1000) facility at DCU is equipped with a Quintel Mask Aligner Model Q4000. Figure 2.5(a) shows a contact printing method when the resist-coated silicon wafer

is brought into physical contact with the glass photomask. The wafer is held on a vacuum chuck and the whole assembly rises until the wafer and mask contact each other. The photoresist is exposed to UV light while the wafer is in the contact position with the mask. Very high resolution is possible in contact printing because of the contact between the resist and mask. The problem with contact printing is that debris trapped between the resist and the mask can damage the mask and cause defects in the pattern. Figure 2.5(b) shows the proximity exposure method, which is similar to contact printing, except that a small gap, 10 to 25 microns wide, is maintained between the wafer and the mask during exposure. This gap minimises mask damage. The proximity exposure method is used in this study which exposed 300 nm UV light source for 9 seconds through a photomask to transfer the pattern. The mask and wafer are aligned and physically brought into soft contact, offering very high resolution while keeping the mask clean. The substrate is exposed to UV radiation through the transparent regions of the photomask causing a change in the photoresist chemical structure. Figure 2.5(c) shows the projection printing methods using imaging optics in between the mask and wafer to avoid mask damage entirely. An image of the patterns on the mask is projected onto the resist-coated wafer which is many centimetres away.

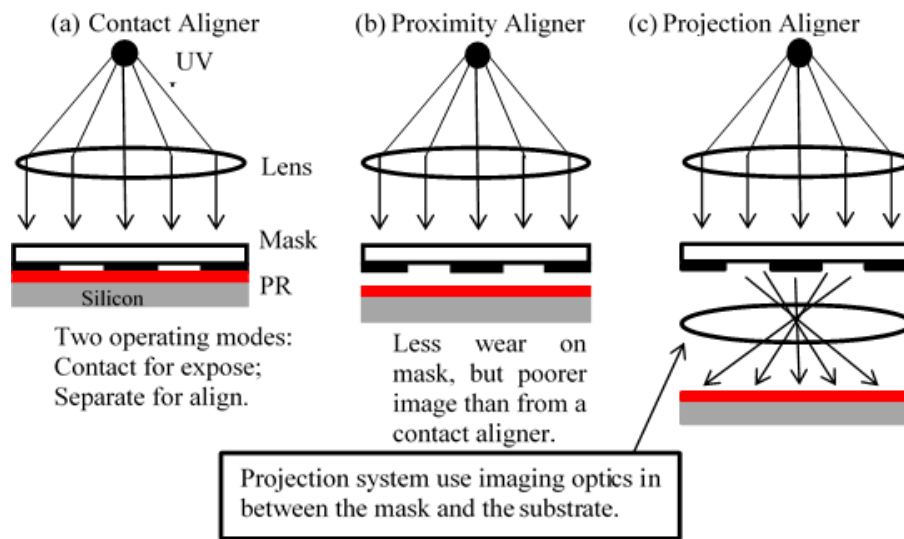


Figure 2.5: Three possible UV exposure methods. (a) Contact printing (b) Proximity printing (c) Projection printing

#### 2.2.1.5 Developer

Figure 2.6 shows the steps after exposure of the mask design is encoded into the photoresist in the form of polymerised and unpolymerised resist. Immersing the substrate into a development solution etches the unpolymerised resist creating a series of voids identical to the mask design. This is developed for approximately 15 seconds at room temperature in 33% (v/v) solution of sodium hydroxide NaOH in water, followed by rinsing thoroughly under water and dried under dry air.

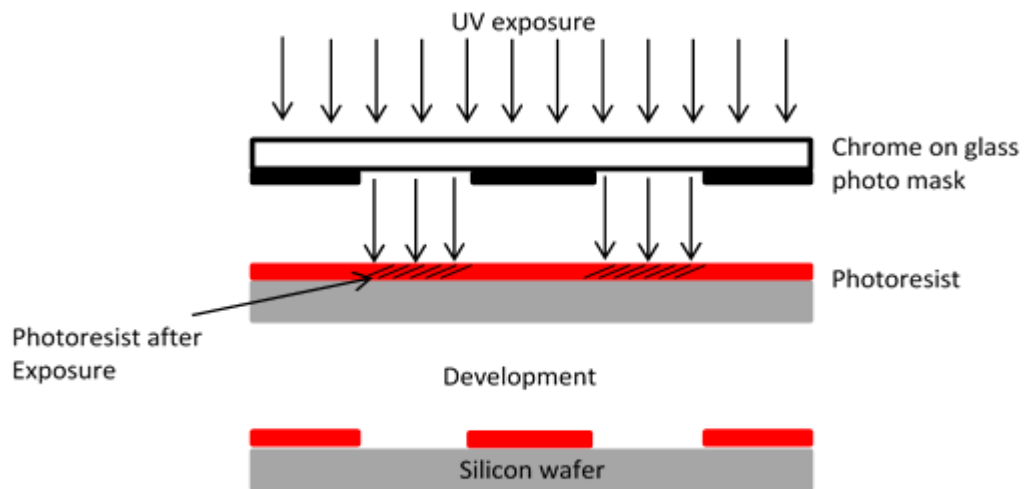


Figure 2.6: Shows the steps after exposure when the mask design is encoded into the photoresist in the form of polymerised and unpolymerised resist and the development

#### 2.2.1.6 Hard-bake

This is the last step before inspection in the photolithographic process. This step is necessary in order to harden the photoresist and improve adhesion of the photoresist to the wafer surface. Figure 2.7 shows the wafer placed on a hot plate with a temperature of 100°C for three minutes. The remaining developer and solvent are evaporated in a controlled manner and adherence between the resist and substrate is increased.

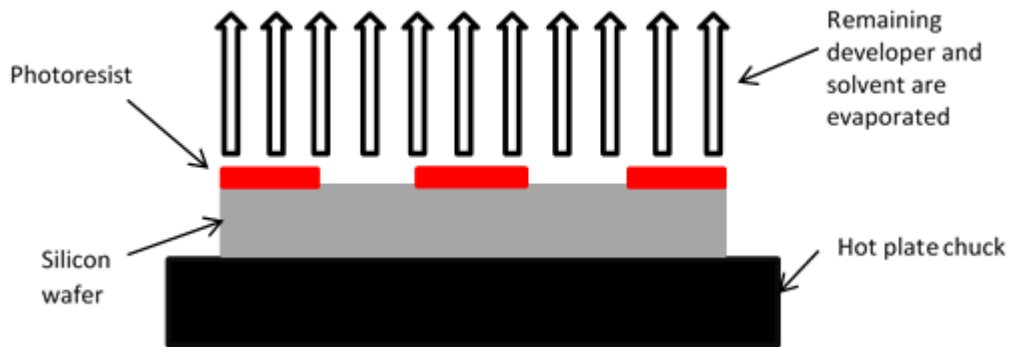


Figure 2.7: Hard-bake steps

#### 2.2.1.7 Sample inspection

The inspection of the samples is very important to make sure that no photoresist particle residues are left on the channels, which would cause reduction of the etch rate, as shown in figure 2.8.



Figure 2.8: Shows the final step of photolithography. The sample was inspected under a microscope

### *2.2.2 Scanning electron microscopy*

Scanning electron microscopy (SEM) is one of the most adaptable types of electron microscopy for surface topography investigation and analysis of materials' chemical composition. SEM was developed to overcome the limitations of the optical microscope, such as lower resolution of 2,000 Å. SEM employs electron beams for imaging rather than visible light as used in conventional optical microscopes. Because of this, it achieves very high resolutions when compared to optical microscopes.

In the scanning electron microscope, a high energy beam of electrons produced by an electron gun is focused in high vacuum into a fine probe that is raster-scanned over the surface to be examined. This electron beam passes through objective lenses and scan coils that deflect vertically and horizontally so that the electron beam can scan the sample surface, as shown in figure 2.9. As the electron interacts with the sample surface, a number of interactions occur which result in the emission of electrons (or photons) from (or through) the surface. These emissions are detected and analysed to give point by point information. The scanning electron microscopes are microscopes with very high magnification (100,000×) which are extensively used for investigating microstructures and chemical composition of surfaces.

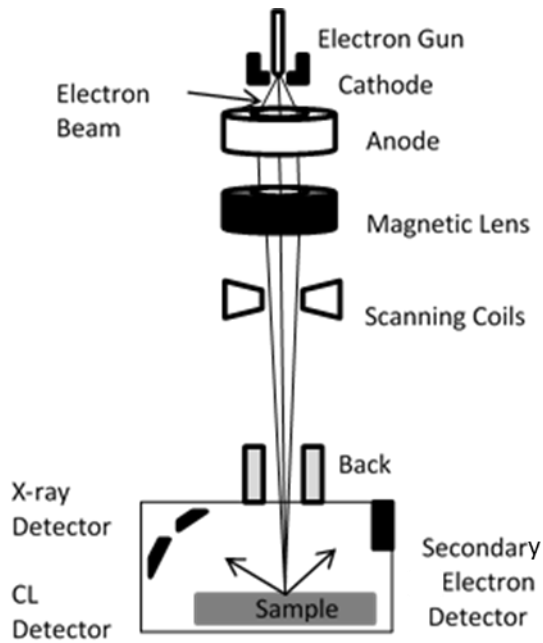


Figure 2.9: Schematic of the SEM, Zeiss EVO LS-15 SEM system

A scanning electron microscope (EVO LS-15, Carl Zeiss, Germany) was used to analyse the processed sample's surface by measuring the depth ( $d$ ) and lateral depth ( $\delta$ ) of sidewalls in the Si etch profile, shown in figure 1.2. This system consists of two chambers under vacuum, (1) the upper chamber containing the electron gun column, and (2) the lower chamber consisting of the sample holder, stage and stage control. By using a differential pumping system with pressure limiting apertures, the lower chamber can be brought to atmosphere without breaking vacuum in the upper chamber.

## 2.3 Plasma diagnostic technique

### 2.3.1 *Optical emission spectroscopy*

One common, non-intrusive, in situ measurement technique for plasma diagnostics is optical emission spectroscopy (OES). With this technique, the intensity of the emission line from the species of interest is monitored. When an electron with sufficient energy hits a particle and causes one of its electrons to jump into a higher shell, the particle is said to be excited. When the particle relaxes and the electron jumps to a lower energy state, a photon with a certain characteristic wavelength is emitted, causing the plasma to glow. The wavelength of the emitted light is determined by the difference between the excited and final energy states of the particle. Each atomic or molecular species has certain allowed energy states, resulting in a unique emission spectrum for each species [34].

In order to understand the variables in the operation of the plasma etch reactors, the first step of the study was to establish the exact composition of the plasma acting on the materials surface and the concentrations of the reactive species. The densities of the reactive species were estimated by the actinometry technique. The Ar emission line at 750 nm, O line at 777 nm and F line at 703 nm were chosen, and their intensities were monitored to check the relative concentrations of O and F atoms in the plasma [35]. These emission lines were selected because they represent electronically excited states that have similar thresholds of excitation

energy. An ultraviolet-visible-near-infrared (UV-vis-NIR) spectrometer (USB 2000, Ocean Optics, USA), which had a resolution of  $\sim 1.5$  nm, was positioned at a quartz window (figure 2.1 and 2.2) to monitor and record the emission spectrum.

### 2.3.2 Actinometry

Actinometry is an optical emission spectrometry (OES)-based technique for determining the radical particle density as a function of the plasma parameters during plasma processing [36], [37]. It is a useful technique for plasma monitoring in semiconductor integrated circuit (IC) manufacturing.

In this technique, a small amount (1% to 5% of total feedstock) of inert gas, known as an actinometer, is introduced into reactive plasma to monitor the actinometer optical emission simultaneously with those of reactive gas. The addition of the inert gas to the feed gas does not affect the emission of the other species present in plasma under different etching gases and conditions.

The intensities of the optical emission of O, F and Ar at 777, 703 and 750 nm, respectively, were recorded as functions of the  $O_2$  concentration in the  $SF_6-O_2$  plasma to satisfactorily calculate the densities of O and F atoms in the plasma. To reach this stage, Ar gas that was regulated to remain at a concentration of 4% was supplied to the  $SF_6-O_2$  plasma to permit the use of the actinometry technique [37], [38]. Ar was chosen as it is inert in nature, and the addition of a small amount (1%

to 5% of the total feedstock) of the inert gas to the feed gas in the chamber did not have a big impact on the emission lines with regard to the plasmas species [38].

The oxygen and fluorine concentrations were measured via optical emission spectroscopy using the actinometry technique, which requires the electron energy distribution function to remain unchanged under the different plasma conditions employed in this work. A Langmuir probe (section 2.3.3) was used to investigate the electron energy distribution function, where the chamber pressure, power and process duration were kept constant and the oxygen concentration was varied from 0% to 60%.

The emission intensity at a particular wavelength is proportional to the concentration of the reactive species in the plasma and other plasma properties [39]. This relationship is expressed as

$$I_x = k_x n_e n_x \quad (2.1)$$

where  $I_x$  is the measured intensity of species x,  $n_e$  is the electron density and  $n_x$  is the concentration of species x. Here,  $k_x$  is the electron impact excitation rate constant, which is given by [40]

$$k_x = \int_0^{\infty} \sigma^x(\varepsilon) f(\varepsilon) \sqrt{\frac{2\varepsilon}{m_e}} d\varepsilon \quad (2.2)$$

where  $\varepsilon$  denotes the electron energy,  $m_e$  stands for the electron mass,  $\sigma^x(\varepsilon)$  is the electron impact excitation cross section and  $f(\varepsilon)$  is the electron energy distribution function normalised to 1 [40].

Previous research had established that light emitted by a species in a plasma is the result of the densities of the excited states, not the overall densities of the species [38]. A constant fraction of the excited species must relax via photon emission. By taking the ratio of the intensities of the actinometer ( $I_{\text{Act}}$ ) and the studied species ( $I_x$ ), we obtained the fundamental relationship of actinometry:

$$\frac{I_x}{I_{\text{Act}}} = \frac{k_x}{k_{\text{Act}}} \frac{n_x}{n_{\text{Act}}} \quad (2.3)$$

The ratio  $k_x/k_{\text{Act}}$  can be assumed to be a constant,  $K$ , provided the collision cross-section of the two excitation reactions are represented by similar functions of the electron energy, or if the electron energy distribution remains constant [39], [41], [42]. If these conditions are met, then actinometry can be used relatively easily to estimate the relative or absolute concentrations of plasma species.

From the ratio of the emission intensities, the O and F densities ( $n_x$ ) were determined with the following equation: [31]

$$n_x = K \frac{I_x}{I_{\text{Ar}}} n_{\text{Ar}} \quad (2.4)$$

where the values of  $I_x$  are the optical emission intensities of F ( $I_F^{703}$ ), O ( $I_O^{777}$ ) and Ar ( $I_{Ar}^{750}$ ) obtained from the OE spectra. The Ar density ( $n_{Ar}$ ) was calculated using the ideal gas law,  $n_{Ar} = P (k_B T)^{-1}$ , where  $P$  is the pressure,  $T$  is temperature and  $k_B$  is the Boltzmann constant. In this work,  $P$  was 1.33 Pa and  $T$  was 300 K. The argon concentration was fixed at 4% of the total gas flow in all of the experiments.

### *2.3.3 Langmuir probe*

The most direct measurements of a plasma are obtained from probes within the plasma chamber. A Langmuir probe is an invasive probe that can be used to determine electron temperature, electron density, electron energy distribution function (EEDF) and plasma potential of a low temperature plasma. The Langmuir probe consists of a small conductor that is placed within the plasma. The basic principle of the Langmuir probe is that the potential of the conductor is varied and the resulting current-voltage trace, or I-V characteristic, is used to determine the properties of the plasma [43]. The Langmuir probe used in this work was a SmartProbe from Scientific Systems with hardware enabling direct values of plasma properties.

Langmuir probes are designed to operate in harsh plasma conditions. A 10–15 mm conducting tip at the end of a conducting rod collects the current for the I-V characteristic. The conducting tip is constructed of a material capable of withstanding high temperatures, typically tungsten or platinum. The conducting

rod is surrounded by an insulating ceramic tube apart from the current collecting. In low-temperature plasmas, Langmuir probes can operate without melting or excessive sputtering at the tip [43], but in high-temperature plasmas the probe is exposed to the plasma for short intervals only (less than one second) to prevent the tip from melting. The ideal I-V characteristics collected from a Langmuir probe are shown in figure 2.10.

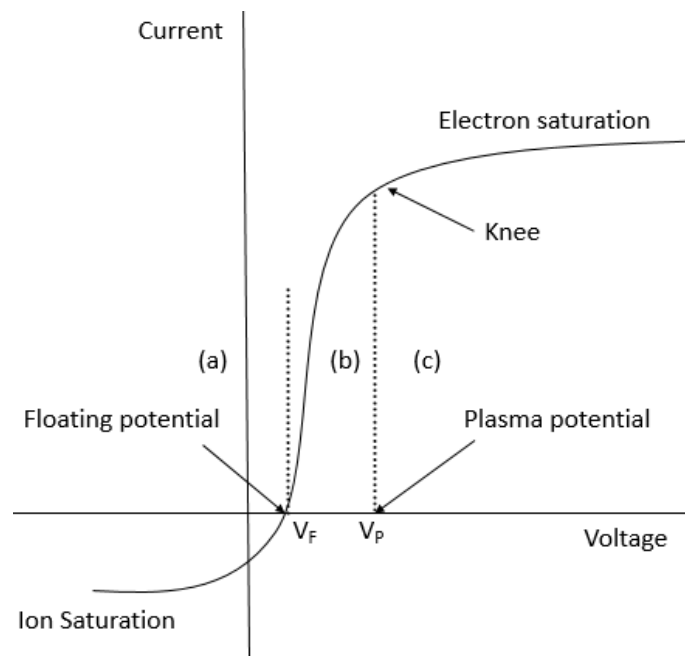


Figure 2.10: Ideal I-V characteristic from a Langmuir probe. Real I-V characteristic curves typically do not have such easily identifiable features

In general, an I-V curve can be separated into three regions according to the floating potential,  $V_f$ , and the plasma potential,  $V_p$ . These regions are as follows: the ion saturation region (a), the electron retardation region (b) and the electron saturation region (c).

(a) Ion current dominates on the left side of the  $V = 0$  point in figure 2.10, because ions are attracted to the probe tip by the low potential. At very negative voltages, the ion current is relatively constant. The sheath area is not affected by the probe voltage. All electrons from the plasma are being repelled by the strong negative charge on the probe. The ion current is determined by the rate of ion arrival at the sheath around the probe tip due to the random movement of ions in the plasma [44].

(b) In this region, increasing the tip potential increases the number of electrons with sufficient kinetic energy to overcome the repulsive electric field at the tip. That results in an increase of the tip current. The point at which the curve crosses the V-axis is the floating potential  $V_f$ . It is the point that the ion and electron currents to the probe tip are equal.

(c) Electron current is dominant at the right side of the  $V_f$  point. The collected current rises throughout the transition region as the probe tip becomes more positive. The shape of the transition region can be used to derive information about the electron temperature and the electron energy distribution of the plasma. When the plasma potential  $V_p$  is reached, the trace takes a sharp turn, known as the “knee” and finishes at a relatively constant electron saturation current. Further increase in the potential (well above the plasma potential) may lead to an increase of the current due to discharge current collection.

More information, including analysis and discussion on Langmuir probes can be found in the “Plasma Diagnostics” chapter of the work by Chen and Chang [43].

The Druyvesteyn formula for calculating  $f(\mathcal{E})$  is

$$f(\mathcal{E}) = \frac{2m}{q^2 A_p} \left( \frac{2q \mathcal{E}}{m} \right)^{1/2} \frac{d^2 I_e}{dV_b^2} \quad (2.5)$$

where  $\mathcal{E}$  is electron energy where is  $\mathcal{E} = V_b - V_p$ ,  $m$  is electron mass,  $q$  is electron charge,  $A$  is area of probe tip and  $I_e$  is electron current. The calculation details can be found and explained in more detail elsewhere [45]. The energy distribution is either Maxwellian or Druyvesteyn, and it can be approximated by straight lines.

The electron density can be calculated based on the EEDF and is

$$n_e = \int_0^{\infty} f(\mathcal{E}) d\mathcal{E} \quad (2.6)$$

## **Chapter 3**

# **Investigation of etch rate and etch profile variation due to additive oxygen and chamber geometry in SF<sub>6</sub>–O<sub>2</sub> plasma**

The Si etching by plasma processing which is widely employed in the semiconductor industry depends on several operational parameters. In this chapter, we have investigated the effect of additive oxygen concentration on the etch rate and etch anisotropy of a silicon substrate in a SF<sub>6</sub>–O<sub>2</sub> plasma. Further, in order to understand how the chamber geometry may affect the etching process, a similar study is carried out in two geometrically different plasma chambers.

### 3.1 Optical diagnostic of SF<sub>6</sub>–O<sub>2</sub> plasma

In order to measure the concentration of F and O during the plasma processing in situ, optical emission spectroscopy (OES) has been carried out. The basic principle of OES has been discussed in chapter 2. In this section, we are demonstrating the OES actinometry technique and how we can use it to obtain the absolute concentrations of oxygen and fluorine in the plasma. It must be noted that actinometry can be applied unless the EEDF remain relatively unchanged for the plasma conditions under examination. The following formula is used to obtain the absolute densities:

$$n_X = K \frac{I_X}{I_{Ar}} n_{Ar} \quad (3.1)$$

where the values of  $I_X$  are the optical emission intensities of F ( $I_F^{703}$ ) or O ( $I_O^{777}$ ), Ar ( $I_{Ar}^{750}$ ) is the intensity of the actinometer and  $K (= k_x/k_{Act})$  is the ratio of the electron impact excitation rate constants of two gases (see equation 2.2).

The Ar number density ( $n_{Ar}$ ) was calculated using the ideal gas law,  $n_{Ar} = P/(k_B T)$ , where  $P$  is the pressure,  $T$  is temperature and  $k_B$  is the Boltzmann constant. The values of  $P$  and  $T$  in this work were 1.33 Pa (10 mTorr) and 300 K respectively. The argon concentration was fixed at 4% of the total gas flow in all experiments. The value of  $K$  is constant only if the electron energy distribution remains constant in the plasma [39], [41], [42]. To make sure the electron energy distribution

function (EEDF) is constant in our plasma, we have used a Langmuir probe [46]. The basic principle of the Langmuir probe and the analysis of current-voltage characteristics have been discussed in chapter 2. The EEDFs of the plasma with various concentrations of oxygen are very similar, particularly in the high energy region from 10 eV and upward. That is important as this energy region is where the excitation cross-sections are dominant. This indicates that the EEDF was essentially unchanged under the different plasma conditions used in our investigation.

Based on equation 2.2, we can assume that the value of  $k_x$  remained constant for all the plasma settings. Consequently, it can be inferred from equation 2.3 that  $K$  is constant. The  $k_x$  values were calculated using equation 2.2, where the electron impact cross-sections and EEDF values for O, F and Ar were obtained from figure 3.2. The calculated values of  $K$  for oxygen and fluorine are 0.78 and 0.47, respectively. The  $K$  values in our case are consistent with the  $K$  values presented in the literature, such as Jenq *et al.* [47] who reported  $K = 0.56$ ; Schabel *et al.* [48] who estimated  $K = 2.84$ ; and Kawai *et al.* [49] who found  $K$  varying from 0.9 to 4.3 in  $\text{CF}_4$  and  $\text{C}_4\text{F}_8$  plasma with estimation of  $K = 2$ .

Figure 3.1 shows the Maxwellian fit to the EEDF data obtained using a Langmuir probe for different  $\text{O}_2\%$ . The cross-sections of Ar ( $\sigma^{750}$ ) and O ( $\sigma^{777}$ ) were taken from the work of Katsch *et al.* [50] and F ( $\sigma^{703}$ ) from Gedeon *et al.* [51] and presented in figure 3.2.

In equation 3.1, we are normalising the intensities of the species of interest with the argon (actinometer). This will make the intensities independent of the electron density in the plasma, under the assumption, the energy dependent shapes of the excitation cross-sections shown in figure 3.2 are similar for all species of interest. Therefore, the ratio of the intensities only depends on the EEDF and concentration [50].

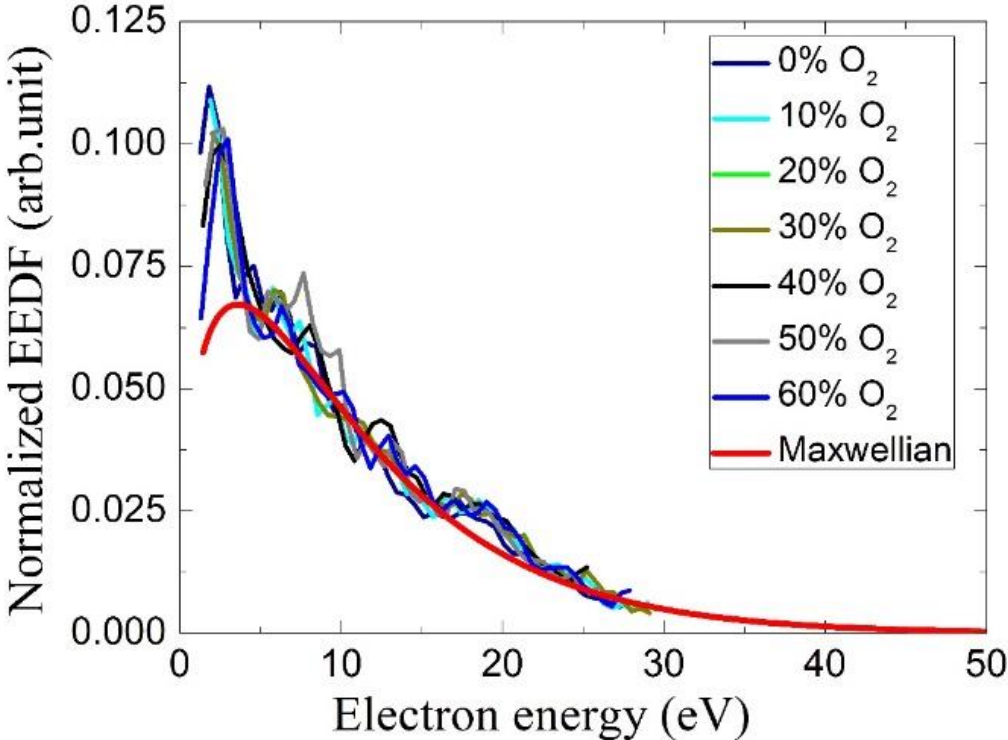


Figure 3.1: Normalised EEDFs for plasmas with different oxygen concentrations as functions of the electron energy

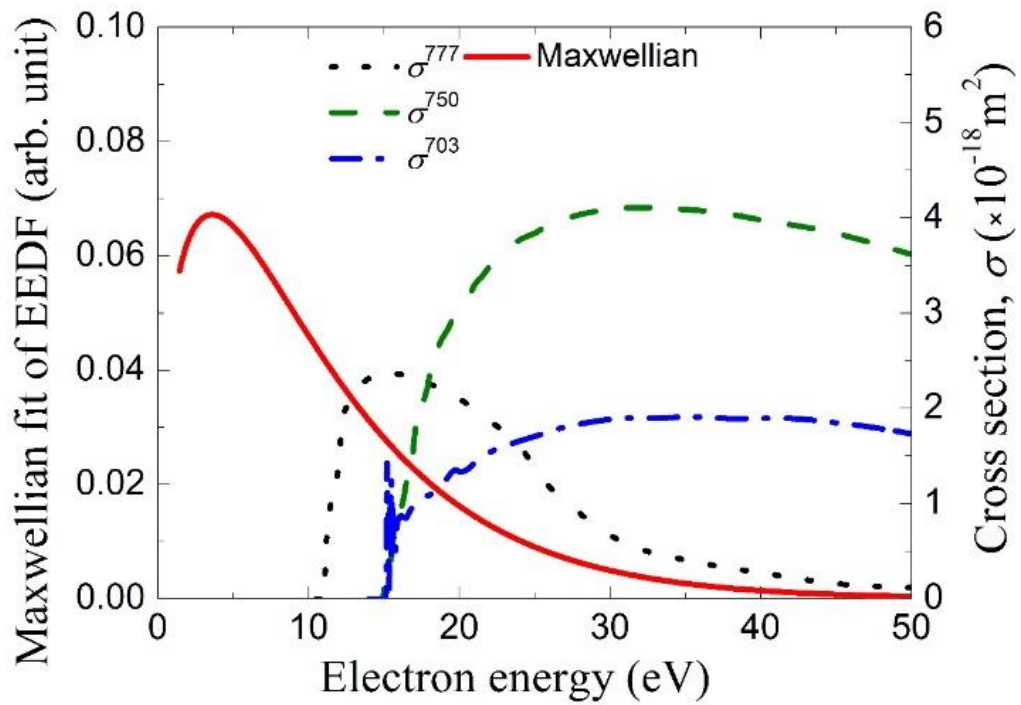


Figure 3.2: Cross-sections of argon ( $\sigma^{750}$ ), fluorine ( $\sigma^{703}$ ) and oxygen ( $\sigma^{777}$ ) as functions of the electron energy

### 3.2 Study of etch rate

We measured etch depth ( $d$ ) and lateral depth ( $\delta$ ) to estimate the etch rate ( $d/\text{time}$ ) and  $\delta/d$  as a function of oxygen concentrations under the same plasma power of 200w and 10mTorr. An experiment is carried out in both plasma chambers named OIP 80+ and OIP 100.

Figure 3.3 shows the plot of etch rate as a function of O<sub>2</sub> concentration. Both chambers exhibit the same trend of etch rate. However, the etch rate in the case of OIP 80+ is around 2.5 times higher compared to the case of OIP 100 because of the different chamber volume. The smaller the volume, the greater will be the energy supplied to the individual particles to cause more effective collisions. Therefore, density increases for the smaller chambers such as OIP 80+ as compared to the OIP 100.

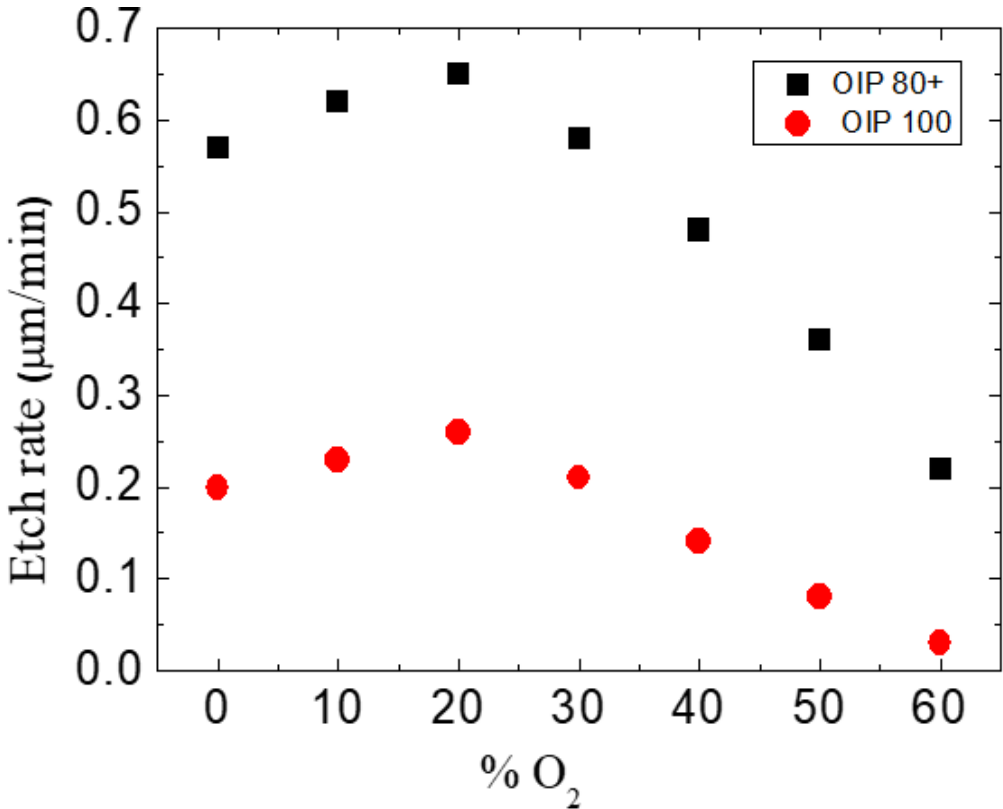


Figure 3.3: Silicon etch rate for the two chambers: OIP 80+ and OIP 100. The squares represent data for the OIP 80+ plasma source, and the circles represent data for the OIP 100 discharge

Table 3.1: List of probable chemical reactions in the CCP dry etch system [52].

<u>Electron-impact ionisation</u>	<u>Production of F from O<sub>2</sub>%</u>
$SF_6 + e \rightarrow SF_5^+ + F + 2e$	$SF_5 + O_2 \rightarrow SO_2F_2 + 3F$
$SF_5 + e \rightarrow SF_4^+ + F + 2e$	$SF_5 + O_2 \rightarrow SO_2F_2 + F_2 + F$
$SF_5 + e \rightarrow SF_5^+ + 2e$	$SF_4 + O_2 \rightarrow SO_2F_2 + 2F$
$SF_4 + e \rightarrow SF_3^+ + F + 2e$	$SF_4 + O_2 \rightarrow SO_2F_2 + F_2$
$SF_4 + e \rightarrow SF_4^+ + 2e$	$SF_3 + O_2 \rightarrow SO_2F_2 + F$
$SF_3 + e \rightarrow SF_2^+ + F + 2e$	$SF_5 + O \rightarrow SOF_2 + 3F$
$SF_3 + e \rightarrow SF_3^+ + 2e$	$SF_5 + O \rightarrow SOF_2 + F_2 + F$
$O_2 + e \rightarrow O^+ + O + 2e$	$SF_4 + O \rightarrow SOF_2 + 2F$
$O_2 + e \rightarrow O_2^+ + 2e$	$SF_4 + O \rightarrow SOF_2 + F_2$
<u>Electron-impact distribution</u>	$SF_3 + O \rightarrow SOF_2 + F$
$SF_6 + e \rightarrow SF_5 + F + e$	<u>Destruction of F</u>
$SF_5 + e \rightarrow SF_4 + F + e$	$SF_5 + F \rightarrow SF_6$
$SF_4 + e \rightarrow SF_3 + F + e$	$SF_4 + F \rightarrow SF_5$
$SF_3 + e \rightarrow SF_2 + F + e$	$SF_3 + F \rightarrow SF_4$
$O_2 + e \rightarrow O + O + e$	$SF_2 + F \rightarrow SF_3$
<u>Dissociative attachment</u>	<u>Surface reaction</u>
$SF_6 + e \rightarrow SF_5^- + F$	$Si + 4F \rightarrow SiF_4$
$SF_5 + e \rightarrow SF_4^- + F$	<u>Surface oxidation</u>
$SF_4 + e \rightarrow SF_3^- + F$	$Si + 2O \rightarrow SiO_2$
$SF_3 + e \rightarrow SF_2^- + F$	<u>Combination</u>
$O_2 + e \rightarrow O^- + O$	$SiO_2 + F \rightarrow SiO_2F$

At lower O<sub>2</sub> concentrations, oxygen increases the production of fluorine through the conversion of SF<sub>6</sub> by reacting with fluorosulphur radicals through SF<sub>6</sub> → SF<sub>5</sub> + F and SF<sub>5</sub> + O → SOF<sub>4</sub> + F and prevent their recombination with fluorine to form SF<sub>6</sub> again. This results in an increase in the etch rate in the plasma.

At certain O<sub>2</sub>%, F and O are nearly equally dominant and prevent further increases of the etch rate. In this condition, SF<sub>5</sub> is fully consumed in the plasma and hence the etch rate attains its peak value. Further increases in O<sub>2</sub>% in the plasma makes oxygen more dominant over fluorine and results in passivation rather than etching. This is due to the recombination of F with SF<sub>5</sub> to form SF<sub>6</sub>. As a result, the etch rate starts decreasing [7], [16]. The etch rate could also decrease due to the polymerisation of silicon where polymerization occurs when Fluorine-contained neutral species (such as SF<sub>6</sub>, SF<sub>5</sub>) and reactive radicals (such as F) will react with the silica to form volatile products and when react with O form siliconoxyfluoride SiO<sub>x</sub>F<sub>y</sub> layer. The polymerisation process prevents F from interacting with the silicon surface and result in decrease in the etch rate as well.

### 3.3 Study of etch profile

In figure 3.4, we plotted the verticality of the sidewall ( $\delta/d$ ) as a function of the oxygen concentration for both plasma systems. Initially, the ratio  $\delta/d$  decreases until we reached 20% O<sub>2</sub> in the plasma. Further increases in the O<sub>2</sub>% results in reduction of  $\delta/d$  due to the passivation of the sidewalls through the formation of SiO<sub>x</sub>F<sub>y</sub> film [53]. Both plasma systems registered the same trends of  $\delta/d$ . However, the value of  $\delta/d$  at 20% O<sub>2</sub> in the case of OIP 100 is 2.5 times higher compared to OIP 80+. For optimum anisotropic etch profile,  $\delta/d \sim 0$ . The minimum value of  $\delta/d$  is obtained at 20% O<sub>2</sub> which is the same condition for obtaining the maximum etch rate in the plasma.

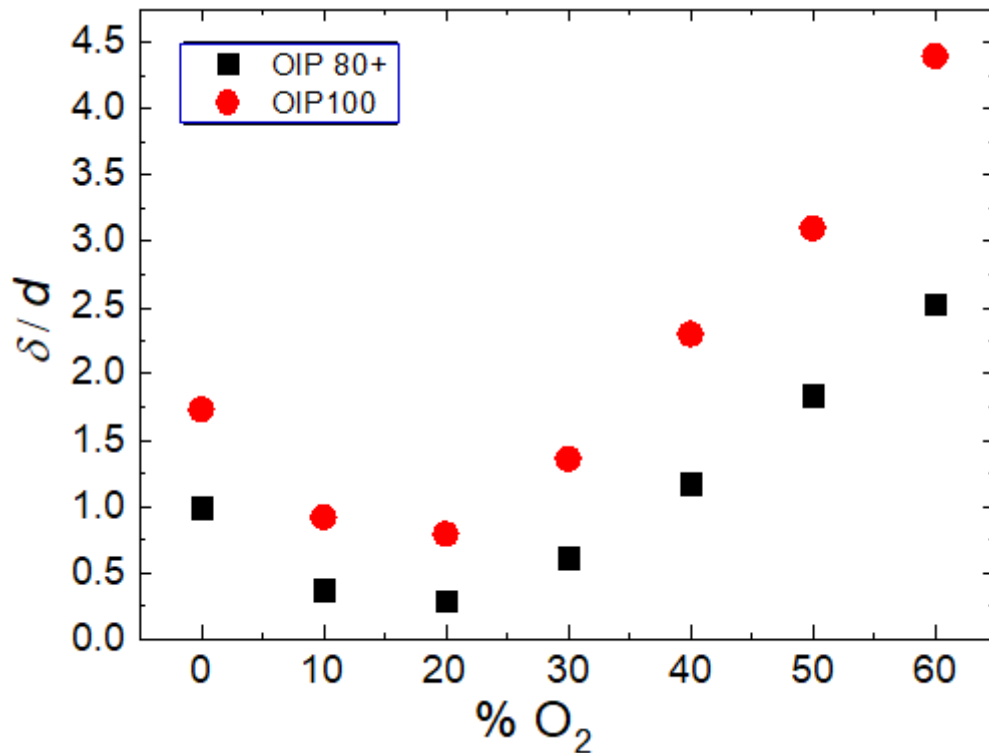


Figure 3.4:  $\delta/d$  versus percentage of  $O_2$  in the  $SF_6$ - $O_2$  plasma of the plasma-etch reactors ( $d$ : depth of sidewall,  $\delta$ : lateral depth of sidewall)

The difference in the etch rate and etch profile for the two different plasma chambers accounts for their differences in geometry. OIP 80+ (1.2) has a smaller ratio of electrode sizes (grounded/power) compared to OIP 100 (1.5). The ratio of electrode sizes can significantly affect the ion energy. This is because self-bias is higher for smaller ratio, and that means more energetic ions can be created in the plasma. The smaller the ratio of the electrode sizes, the greater is the ion bombardment. That is why the etch rate of OIP 80+ is greater than that of the OIP 100.

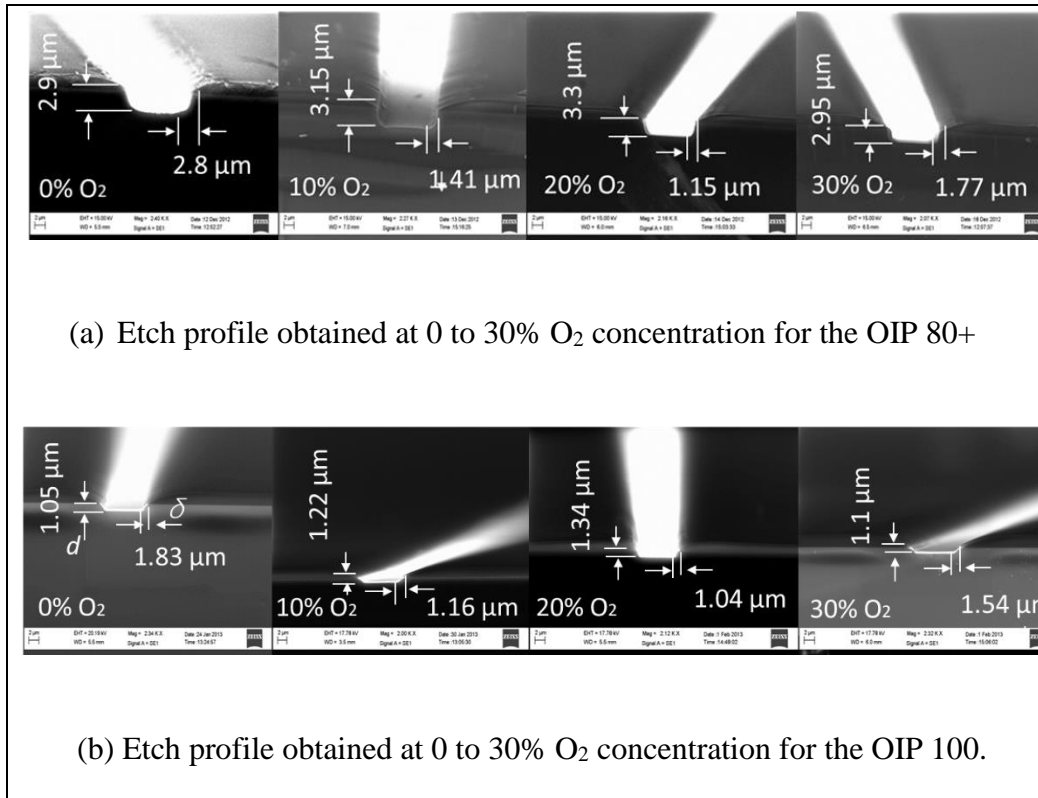


Figure 3.5: A typical SEM cross-section micrographs, (a) Etch profile obtained at 0 to 30% O<sub>2</sub> concentration for the OIP 80+, (b) Etch profile obtained at 0 to 30% O<sub>2</sub> concentration for the OIP 100.

The effect of the O<sub>2</sub> concentration on etch rate and etch profile of the silicon wafer surface is investigated by using scanning electron microscopy (SEM). Figure 3.5a shows a typical SEM picture of a trench on a silicon wafer surface for the OIP 80+, and Figure 3.5b shows a typical SEM picture of trenches on a silicon wafer surface for the OIP 100. On these micrographs we measure the etch depth ( $d$ ) and lateral depth ( $\delta$ ) to calculate etch rate and the ratio between  $\delta$  and  $d$ , as function of the O<sub>2</sub> fraction in the SF<sub>6</sub>-O<sub>2</sub> plasma with similar parameters. The  $\delta/d$  for

different plasma conditions are plotted in figure 3.4. An experiment is carried out in both plasma chambers named OIP 80+ and OIP 100.

### **3.4 Study of atomic oxygen and fluorine concentrations in the plasma**

The intensities of the atomic oxygen and fluorine emission are related to the O and F densities in their ground state [54], [55]. The ratio of the intensities of O and F to the intensity of the Ar emission line are shown in figures 3.6(a) and 3.6(b). These relative intensities allowed us to determine the absolute densities of O ( $n_O$ ) and F ( $n_F$ ) using equation 3.1. Here we ignored the collisional quenching effects, as all our experiments have been performed at a fixed pressure, 10 mTorr. The contribution of dissociation excitation to the emission at 777 nm is not included in our analysis. Therefore, our results over-estimate the values of  $n_O$  and  $n_F$  and should serve as the upper limits of  $n_O$  and  $n_F$ . we have carried out our experiment with single testing for densities of fluorine, oxygen, and electron as a function of oxygen concentration.

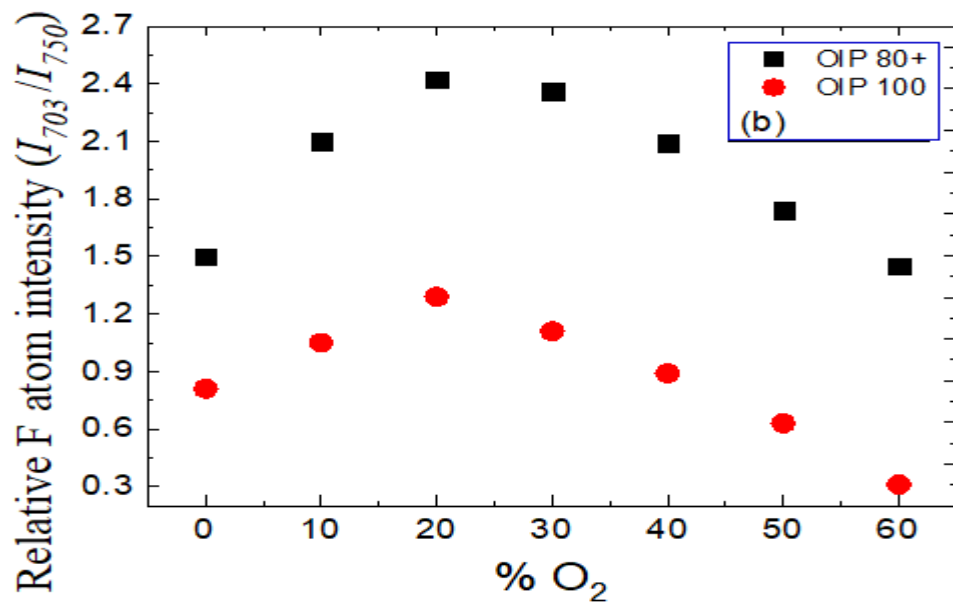
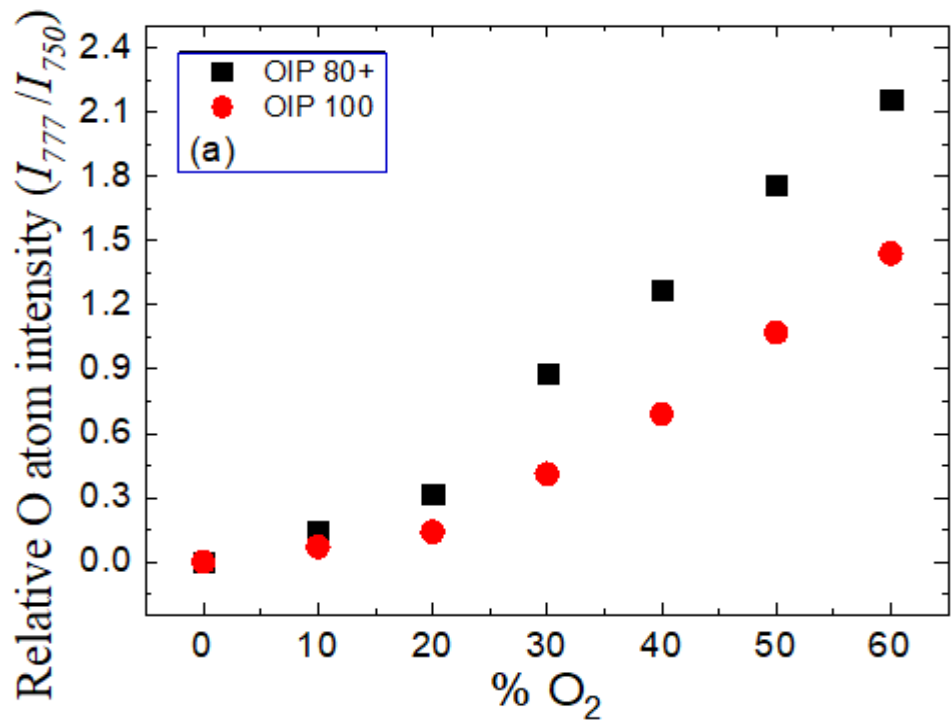


Figure 3.6: (a) Relative O atomic intensity ( $I_{777}/I_{750}$ ) and (b) relative F atomic intensity ( $I_{703}/I_{750}$ ) as a function of O<sub>2</sub> fraction measured in OIP 80+ and OIP

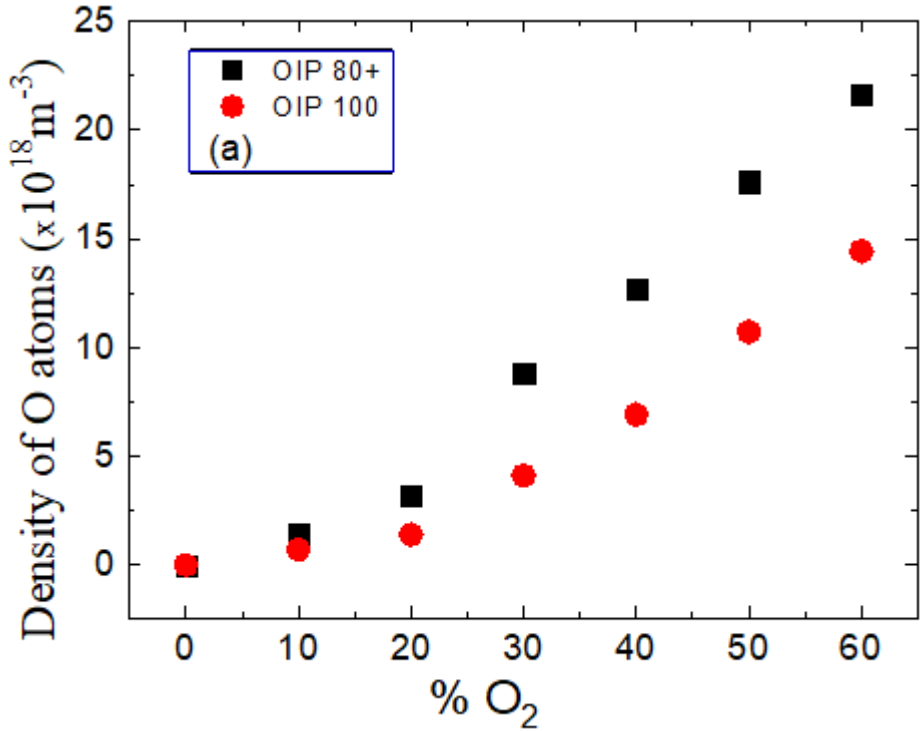
Figure 3.7 shows the absolute densities  $n_O$  and  $n_F$  as a function of  $O_2\%$ . Both densities increase with  $O_2\%$  until we reached the level of 20% oxygen in the plasma. Above  $O_2$ -20%, the F density starts dropping, whereas O density continuously increases with  $O_2\%$ .

Initially ( $O_2 < 20\%$ ), F density increases due to the formation of F through the reaction between  $SF_5$  and O;  $SF_5 + O \rightarrow SOF_4 + F$  until it reaches its peak value at  $O_2$ -20%. For  $O_2 > 20\%$ , the F density decreases due to the dominance of O over F in the plasma, which results in the recombination of  $SF_6$  in the plasma;  $SF_5 + F \rightarrow SF_6$  [56], [57]. The trend of F density is consistent with the trends obtained for etch rate and  $\delta/d$ . The peak F density, peak etch rate and the lowest value of  $\delta/d$  occurred at the same plasma condition when  $O_2$  is 20%. The F density is 1.9 times higher in OIP 80+ compared to OIP 100 because of its smaller volume and ratio of the electrodes' size.

Figure 3.7(a) shows the graph between O densities as a function of  $O_2\%$ . Initially (up to  $O_2$ -20%), the O density increases at a very slow rate, but later ( $O_2 > 20\%$ ) at a much faster rate due to the reduction in the F densities as indicated in figure 3.7(b). This will create an oxygen-rich plasma in which fluorine recombines to form  $SF_6$ ;  $SF_5 + F \rightarrow SF_6$  [56]. On the other, oxygen density increases due to the formation of atomic oxygen through electron impact ionisation, electron impact dissociation, and dissociative attachment, as presented in table 3.1. The O density

in OIP 80+ is 2.1 times higher compared to OIP 100 because of the smaller volume and ratio of the electrode sizes in case of OIP 80+.

However, these experimental results are limited to a condition of constant power of 200W. The full performance of the chambers should be compared by investigating the power required to maintain the same amount of density in the plasma. This may conclude that the chamber geometry plays an important role in changing the densities of F and O atoms [56] in a plasma and to choose a chamber that produce a required amount of species to achieve optimal etch conditions.



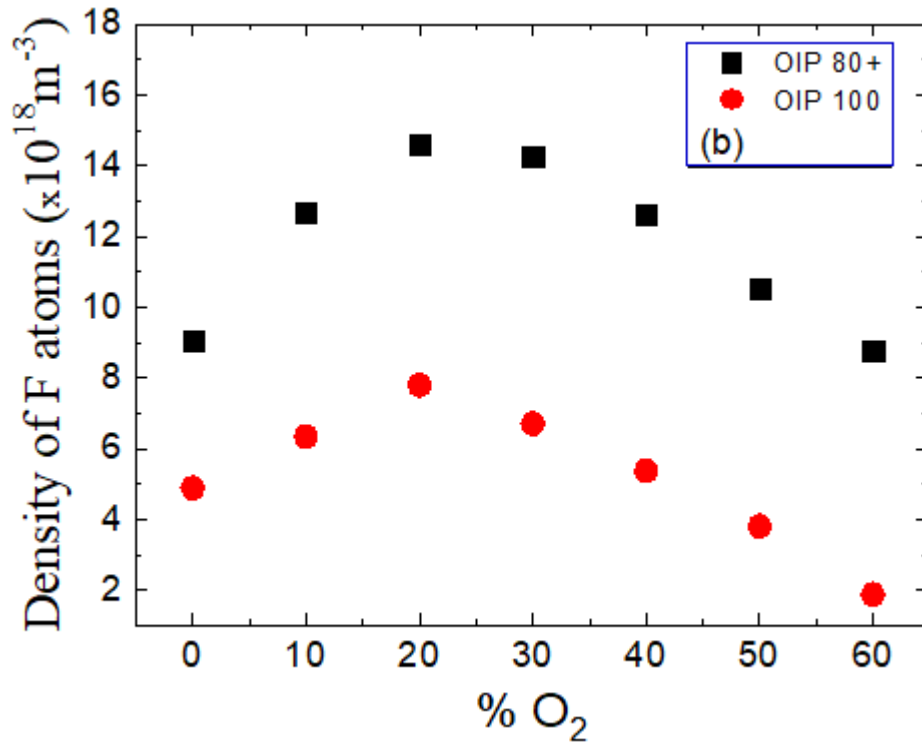


Figure 3.7: Densities of (a) F atoms and (b) O atoms as functions of the O<sub>2</sub> fraction in SF<sub>6</sub>-O<sub>2</sub> in the plasma chambers. The squares represent data for the OIP 80+ chamber, and the circles represent data for the OIP 100 chamber

### 3.5 Study of electron density

The electron density was measured using a Langmuir probe. The technique has been described in chapter 2. The probe was placed at the centre of the discharge all the time. Figure 3.8 shows that the electron density as a function of O<sub>2</sub>% for both OIP 80+ and OIP 100 plasma systems. The plasma conditions such as pressure and power are kept constant. We obtained the same trends of electron density for both chambers. However, the electron density measured in OIP 80+ is

about two times higher compared to the electron density measured in OIP 100. The electron density initially increases up to  $O_2 = 20\%$  and then decreases in the plasma.

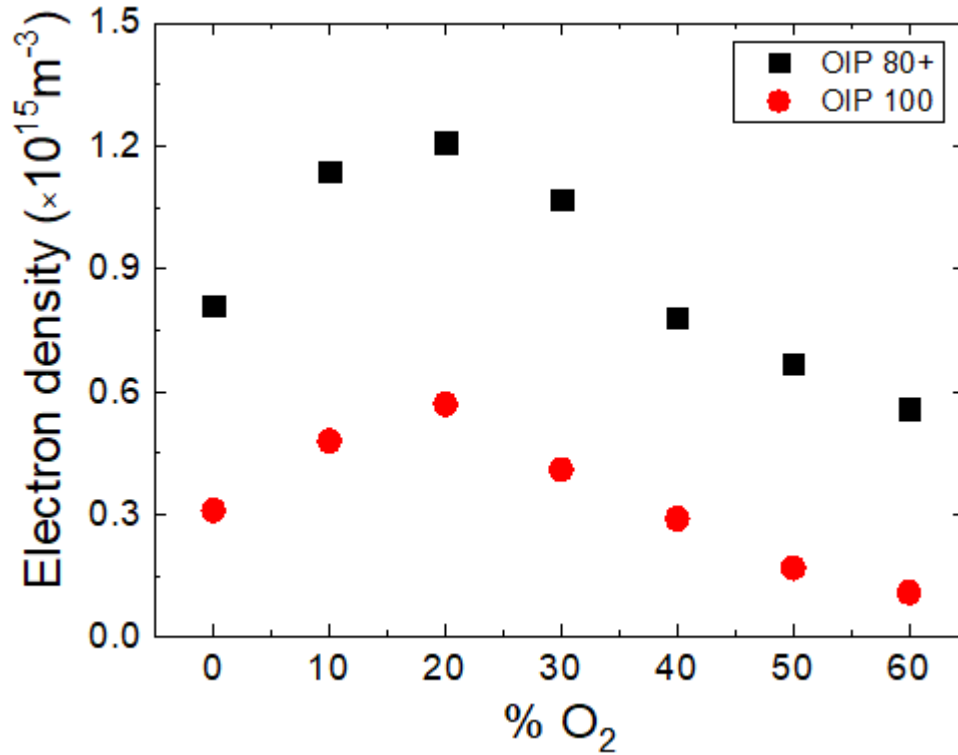


Figure 3.8: Electron density as a function of the  $O_2$  fraction in  $SF_6-O_2$  in the plasma chambers. The squares represent data for the OIP 80+ chamber, and the circles represent data for the OIP 100 chamber

As  $O_2$  concentration increases in the plasma, the concentration of F atoms and electron density also increases due to the electron impact ionisation and electron impact dissociation, as shown in table 3.1.

## **3.6 Comparison of etch rates between OIP 80+ and OIP 100**

The ratio of the volume of OIP 80+ to the OIP 100 is 1:2.16 whereas the ratio of the ground electrode size in OIP 80+ to that in OIP 100 is 1:1.25. We have further analysed the etch rates and fluorine densities between OIP 80+ and OIP 100 as a function of O<sub>2</sub>%. The experimental data is plotted in figures 3.9 and 3.10. We found that etch rate in OIP 80+ is nearly three times the etch rate obtained in the case of OIP 100. However, this is only consistent up to the definite amount of O<sub>2</sub> level i.e., 30% in the plasma. The etch rate goes up exponentially as we increase O<sub>2</sub> concentration above 30%. A similar feature is obtained in case of densities where it is two times higher than the density obtained in the OIP 100 system. After that, we have seen significant rises in the densities of OIP 80+ as compared to that in OIP 100. Both etch rates and densities are consistently increasing with each other.

For O<sub>2</sub> < 30%, the F densities in OIP 80+ are higher (two times) because of its smaller volume and smaller ratio (1.2) of the electrodes compared to the OIP 100 (1.5). A smaller volume holds more energetic particles that results in an increase in the effective collisions. This results in a higher density and hence a higher etch rate in the plasma. Also, the self-bias is higher for OIP 80+ as compared to the OIP 100. However, the results (O<sub>2</sub> > 30%) in figures 3.9 and 3.10

show that the F densities in OIP 80+ are now exponentially higher compared to the OIP 100. This means that O<sub>2</sub> concentration in OIP 80+ is less dominant compared to the OIP 100, leading to the higher level of fluorine density for higher level O<sub>2</sub>%.

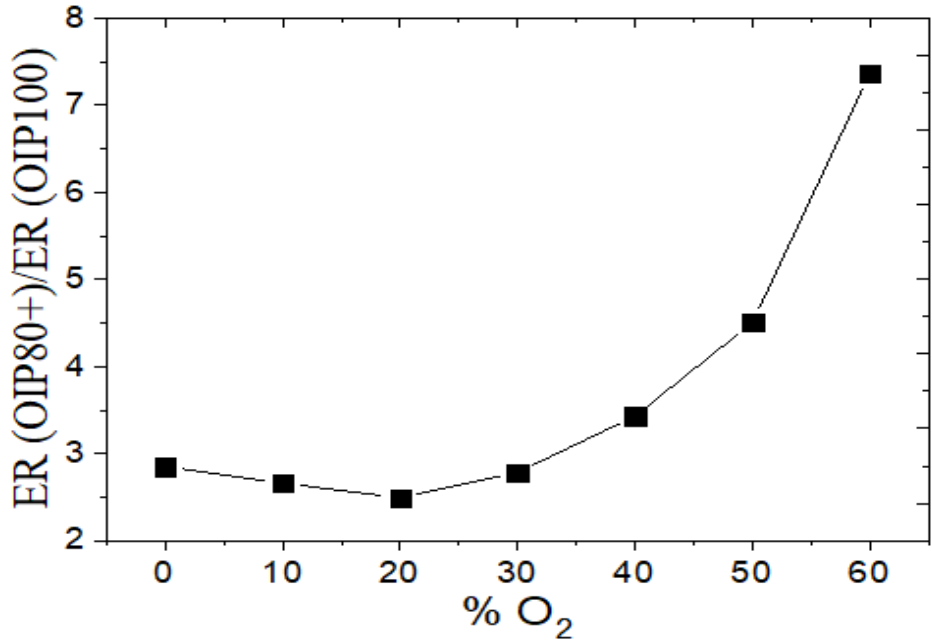


Figure 3.9: Ratio of etch rates between OIP 80+ and OIP 100 vs O<sub>2</sub>%

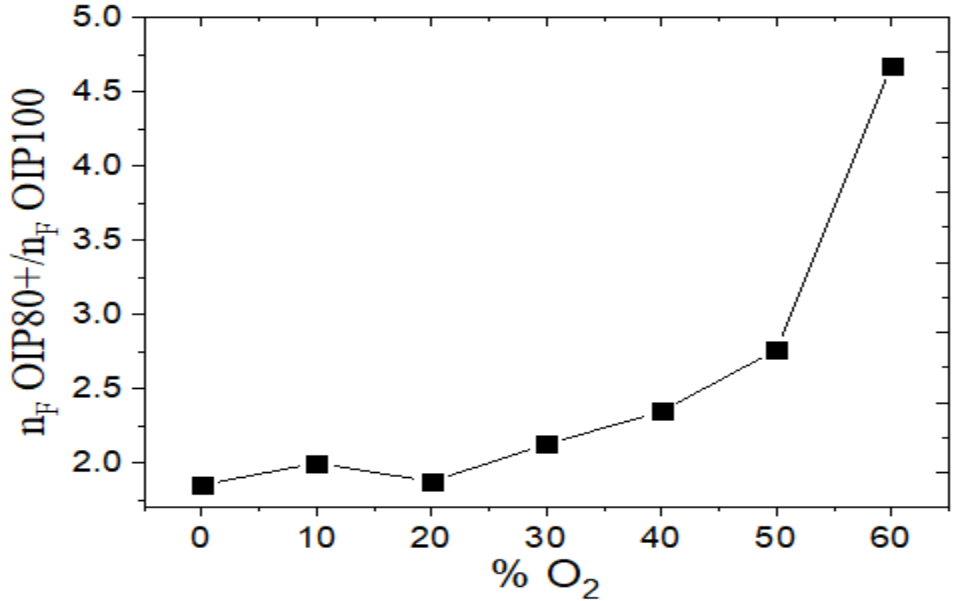


Figure 3.10: Ratio of densities between OIP 80+ and OIP 100 vs O<sub>2</sub>%

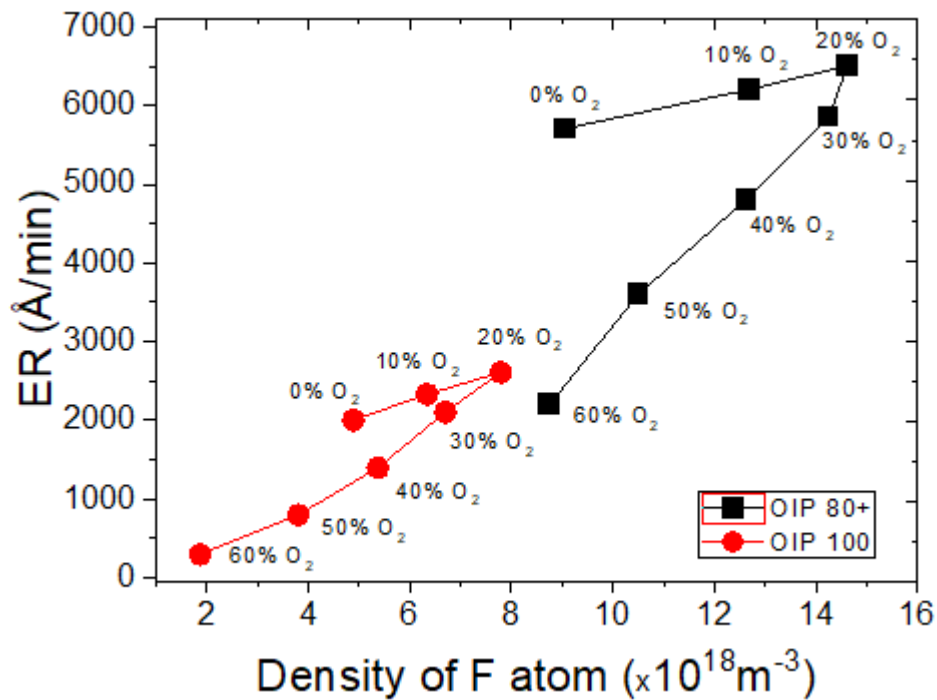


Figure 3.11: Etch rate vs fluorine density for OIP 80+ and OIP 100

In figure 3.11, we have presented the etch rates as a function of F densities in both OIP 80+ and OIP 100. The graph shows that how the density and etch rates are increasing for O<sub>2</sub> level 0–20% and then decreasing when O<sub>2</sub> > 20%. This is consistent with both of the chambers. The decrease in F densities and etch rates is due to the dominance of the O<sub>2</sub> in the plasma, as discussed earlier.

### 3.7 Conclusion

We studied the silicon etch process in the SF<sub>6</sub>–O<sub>2</sub> plasma produced in two geometrically different plasma chambers, OIP 80+ and OIP 100. Both chambers give the same etch profile as a function of oxygen concentration under the same

plasma conditions (10 mTorr and 200 W). However, the etch rate values are higher for the smaller chamber, OIP 80+, because it holds more energetic particles that result in increasing effective collisions and hence densities. The peak values of etch rates for both chambers happen at the same O<sub>2</sub> level (20%). However, this operating condition resulting in a peak etch rate may differ if the experiment is conducted at different pressures and/or in different chambers.

## **Chapter 4**

# **Theoretical analysis of the ion energy distribution and relationship between etch rate and density in SF<sub>6</sub>–O<sub>2</sub> plasma**

### **4.1 Theoretical analysis of ion energy distribution in RF plasma**

Ion energy plays an important role in achieving the desired profile. This is because the sheath adjacent to the substrate affected the ion flux and ion energy and impacted the surface. The sheath voltage is the main parameter that can alter the path of the ions approaching the substrate and that can result in isotropic profile in the etching [58]. The sheath thickness depends on the sheath electric field and the Debye length, which can be controlled by varying the amplitude of the RF voltage or by changing the DC bias at the substrate electrode. Using these operating parameters, we can optimise the ion energy at the substrate and hence the etching profile.

The sheath voltage waveform is periodic in the case of RF plasma and, therefore, the energy of an ion ( $E$ ) hitting the target depends on the phase angle  $\theta$  at which the ion enters the sheath [59]. In a low-frequency regime i.e.,  $\tau_{\text{ion}}/\tau_{\text{rf}} \ll 1$ ,  $\tau_{\text{ion}}$  is the ion transit time through sheath and  $\tau_{\text{rf}}$  is the time period of the RF cycle. Under this condition, the ion energy distribution,  $f_i(E)$ , is given by [59]:

$$f_i(E) = \frac{1}{\pi} ((eV_{dc})^2 - E^2)^{-\frac{1}{2}} + \frac{1}{2} \delta(E) \quad (4.1)$$

where  $E=eV_{dc}\sin\theta$  and  $V_{dc}$  is the DC bias voltage. The DC self-bias voltage plays an important role in etching. For instance, a higher DC bias leads to an increase in ion energy.

Using equation 4.1, we calculated the ion energy distribution,  $f_i(E)$ , for different values of DC bias, and the results are plotted in figure 4.1. The  $f_i(E)$  obtained is bimodal in nature where the two peaks correspond to the maximum and minimum sheath drops where the voltage varies slowly.

We found that the energy spread is highest for 350 V case and lowest for the 40 V case. DC bias can be influenced with external parameters such as oxygen level and pressure. Lower DC bias results in a smaller energy spread in the  $f_i(E)$ , whereas higher DC bias results in a bigger energy spread. On the other hand, the ion population corresponding to the maximum energy peak falls down with an increase in the DC bias.

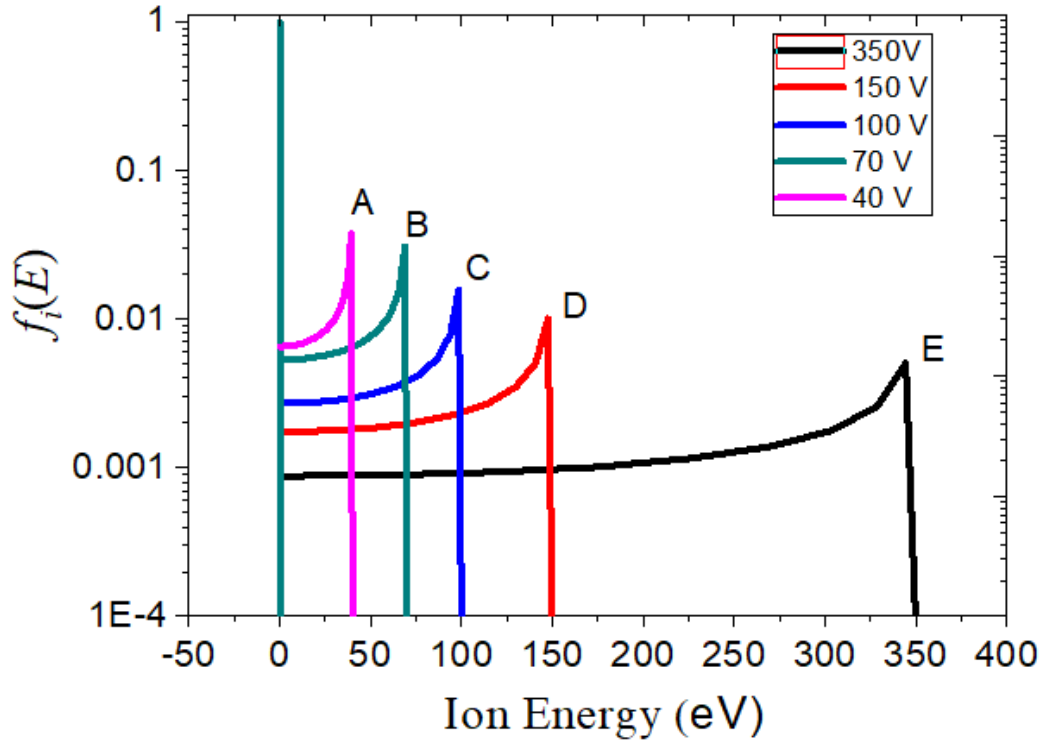


Figure 4.1: Ion energy distribution,  $f_i(E)$ , vs energy for different DC bias

In figure 4.2, we plotted the peak values of the ion population ( $IP$ ) versus ion energy corresponding to the points A–E in figure 4.1. The result shows the nonlinear trend between the ion population and energy, confirming the inverse correlation between the two parameters. We used the nonlinear curve fitting method and obtained an equation, as given below:

$$IP = 0.007 + \left( \frac{0.14}{(1+0.014 E)^3} \right) \quad (4.2)$$

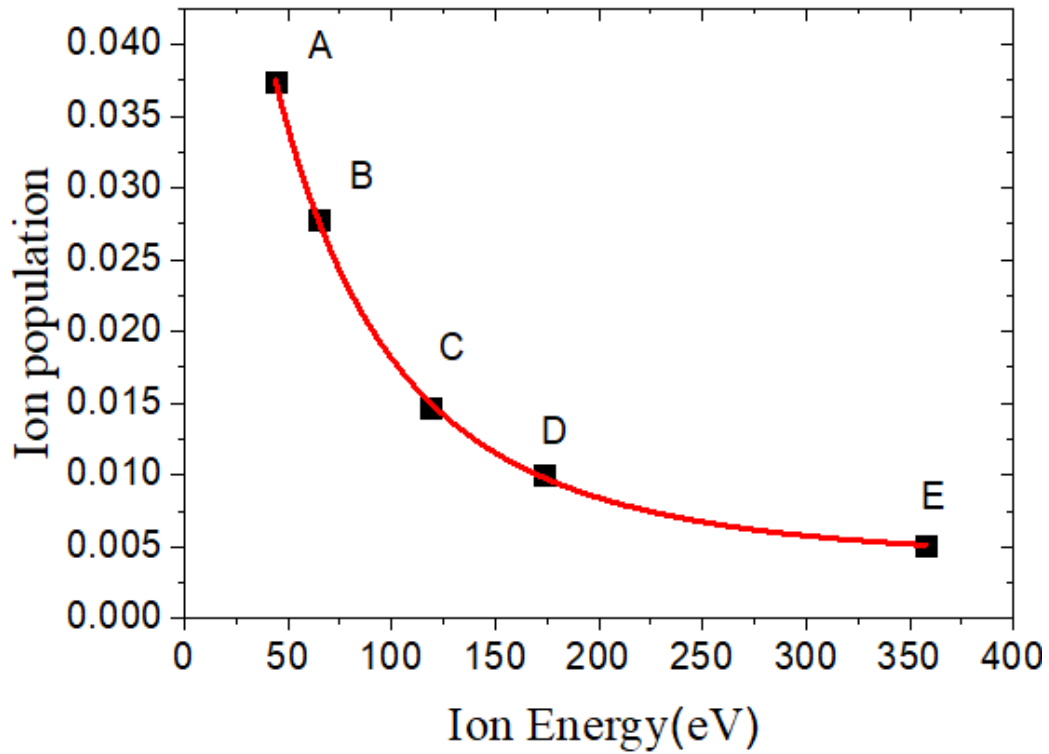


Figure 4.2: Ion population vs ion energy

According to figure 4.2, the ion population is inversely related to the ion energy spread. The lower the DC bias, the greater will be the sheath drop, and hence, the greater will be the plasma density. The peaks of the ion populations corresponding to the different DC biases shows a trend which is given by equation 4.2. The ion energy distribution,  $f_i(E)$ , in RF plasma and its broadening can provide important information about the peak etch conditions. For example, DC bias can be influenced with external parameters such as oxygen level and pressure. Lower DC bias results in a smaller energy spread in the  $f_i(E)$ , whereas higher DC bias results in a bigger energy spread. However, for high density plasma which is typically

used in commercial settings, the DC bias has to be chosen in a way to control the ion energy and protect the surface from any physical or chemical damage.

## 4.2 Relationship between the etch rate and fluorine densities

A broad understanding about the reaction of fluorine and oxygen with silicon is important for the desired etch rate and profile. A study by Flamm *et al.* [60] provides detailed information about the reaction of fluorine with silicon where the etch rate of fluorine is given by the following equation:

$$ER = 2.91 * 10^{-12} * n_F * \sqrt{T} * EXP\left(\frac{E_{act}}{K_B T}\right), \quad (4.3)$$

$ER$  is etch rate,  $T$  is fluorine temperature,  $n_F$  is fluorine density,  $K_B$  is Boltzmann constant and  $E_{act}$  is activity energy. The fluorine temperature for pure  $SF_6$  plasma is typically at 500 K [57] and activation energy is about 1.68. Therefore, the etch rate is mainly depending on the F density in the plasma. This feature has been studied experimentally in chapter 3. In figure 4.3, we have plotted the data to show the locus of silicon etch rate  $ER$  and F atom density as the function of % $O_2$  in a  $SF_6$ - $O_2$  plasma. The data is consistent for both OIP 80+ and OIP 100.

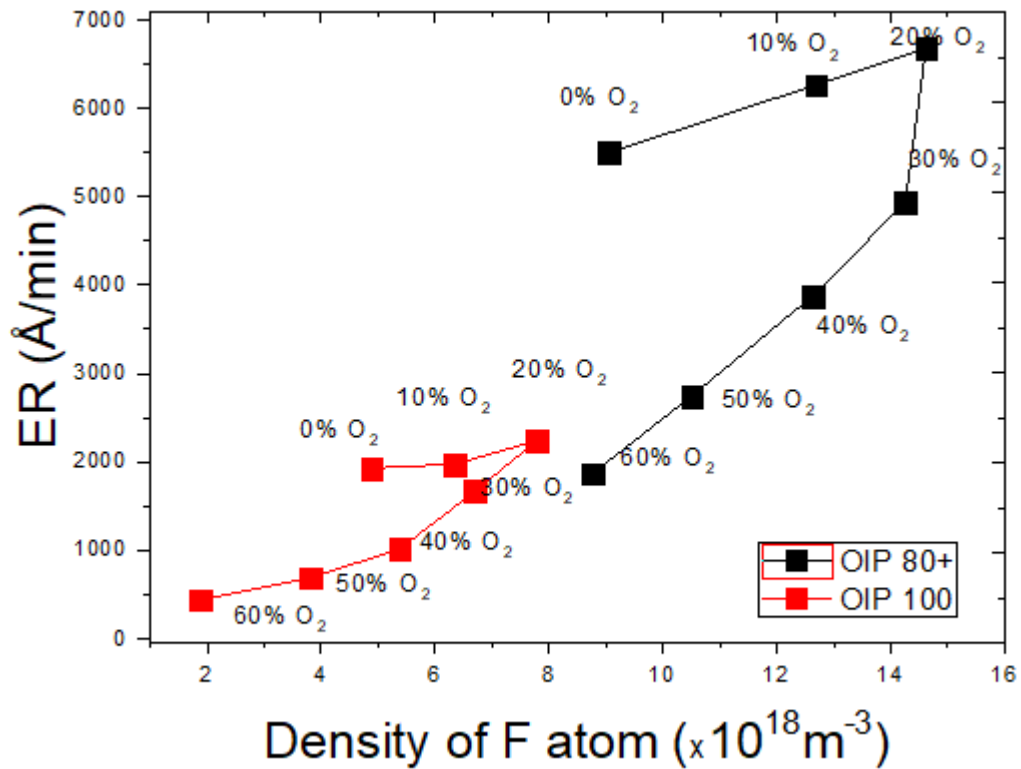


Figure 4.3: Locus of silicon etch rate  $ER$  and F atom density as the function of  $\%O_2$  in a  $SF_6-O_2$  plasma

This feature of the graph is similar to the one presented by Mogab *et al.* in 1979 [61] for  $CF_4/O_2$  plasma. Mogab *et al.*'s graph, presented below, has three main features: (1) Both  $ER$  and F density increases with  $O_2$  level up to 16%; (2)  $ER$  decreases but F density increases when  $O_2$  level varies between 16% to 30%; (3) Both  $ER$  and F density decreases above 30%  $O_2$  level.

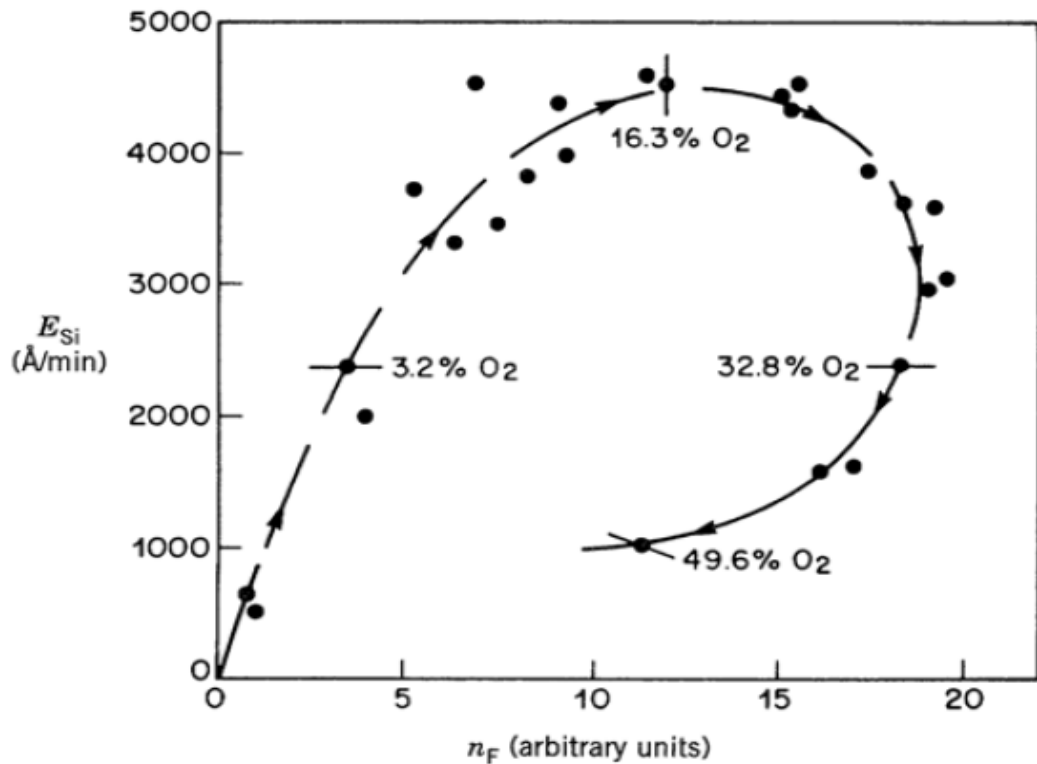


Figure 4.4: Etch rate of Si versus F atom density. Arrows indicate the direction of increasing  $O_2$  concentration in the feed [61]

In our experiments as shown in figure 4.3, the transition region is missing where the ER decreases and F density increases. This is because our experiments were carried at the 20% and the 30%  $O_2$  level and due to that we could not obtain the data in between. The first and third regime of the graph is generally agreed, because with an increase in  $O_2$  level, initially the F density increases and that results in the increase in the etch rate. However, in the third regime, the  $O_2$  gets more dominant over fluorine and results in passivation rather than etching. This is due to the recombination of F with  $SF_5$  to form  $SF_6$ . As a result, the etch rate starts decreasing [16]. The etch rate could also decrease due to the polymerisation

of silicon, especially on the etched trenches and sidewalls. The polymerisation process prevents F from interacting with the silicon surface and result in decrease in the etch rate as well. The second regime of increasing F density and decreasing the etch rate is due to the chemisorption of O atoms on the SF<sub>6</sub> and hence it forms an oxide-like layer resulting in reduction in the etch rate. On the other hand, F density continuously increases in the regime.

## **Chapter 5**

# **Investigation of etching optimisation in capacitively coupled SF<sub>6</sub>-O<sub>2</sub> plasma**

In chapter 3, we experimentally investigated the anisotropic etch profile in two geometrically different capacitively coupled plasma sources (OIP 80+ and OIP 100). The results obtained indicated that the etch profile varies as a function of F and O densities in the plasma chamber. The peak etch rates for both chambers were obtained at 20% oxygen concentration under the given plasma conditions i.e., at constant pressure (10 mTorr) and power (200 W). However, the peak etch rate condition for a given plasma reactor may change with other parameters, such as O<sub>2</sub>%, DC bias, power and operating pressure. This motivates us to further extend our research study and perform a detailed investigation of the etch process in the SF<sub>6</sub>-O<sub>2</sub> plasma.

## **5.1 Ion energy distribution for RF plasma and its comparison with the experimental investigations**

In our experiments, we noted the readings of the DC bias voltage by varying the O<sub>2</sub>% and pressure. Figure 5.1 and figure 5.2 shows DC bias vs pressure and O<sub>2</sub>% respectively. The DC bias decreases exponentially with pressure while it increases linearly with O<sub>2</sub>%. The decrease in the ion energy is due to the increase in collisions at higher pressures, and therefore, the ions losing energy. On the other hand, the ion energy is inversely proportional to the mass ( $\propto m^{-1/2}$ ) and increase in O<sub>2</sub>% is solely due to the increase in the plasma potential. This is because we are operating in a situation where conditions which can alter self-bias voltage in our plasma are fixed. As a result, the DC bias voltage increases with O<sub>2</sub>% [62]. The self-bias voltage may change under alterations in the conditions, such as if we change the ratio between the surface areas of the ground and powered electrodes, chamber pressure, RF forward power and type of gas.

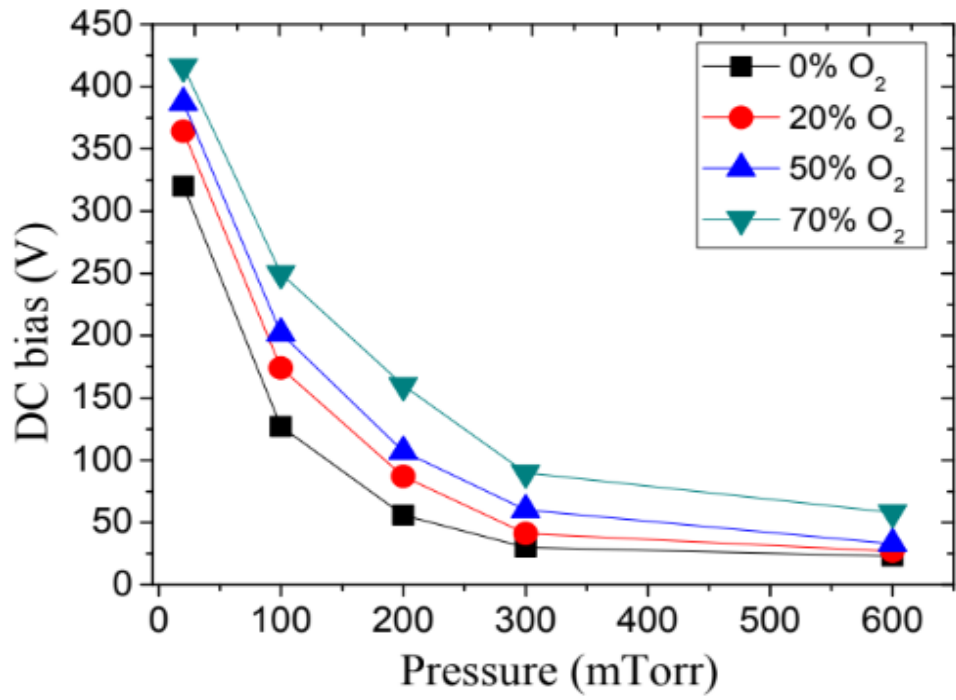


Figure 5.1: DC bias vs pressure

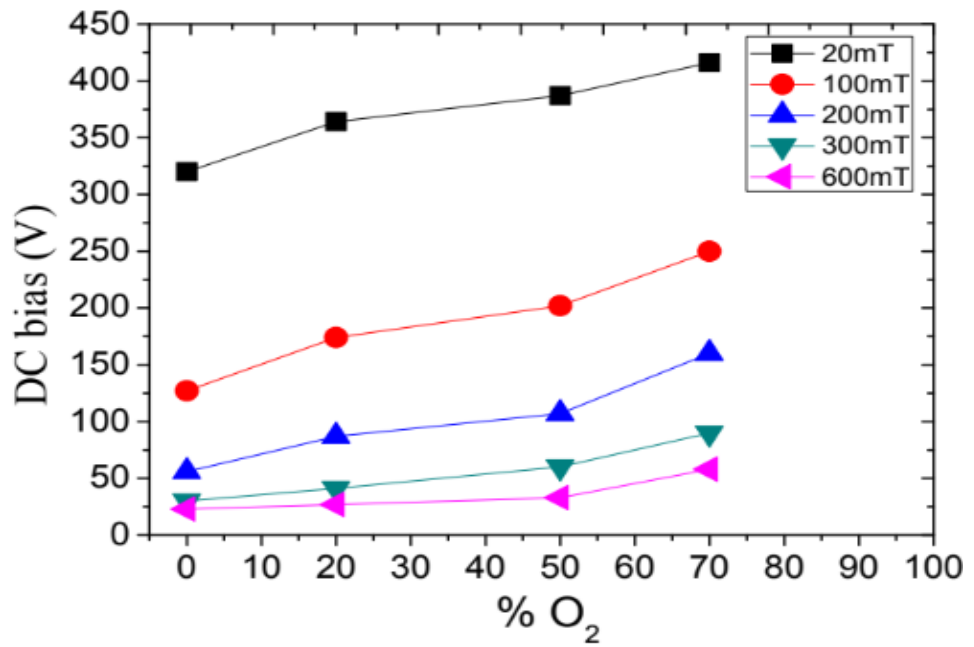


Figure 5.2: DC bias vs %O<sub>2</sub>

In figure 5.3, we have presented the DC bias data points as a function of pressure corresponding to the peak etch rate condition. Clearly, the DC bias for peak etch condition is lower for higher pressure and high O<sub>2</sub>% and higher for lower pressure and low O<sub>2</sub>%. This may be due to the decrease in the ion energy at high pressure because of higher collisions in the plasma.

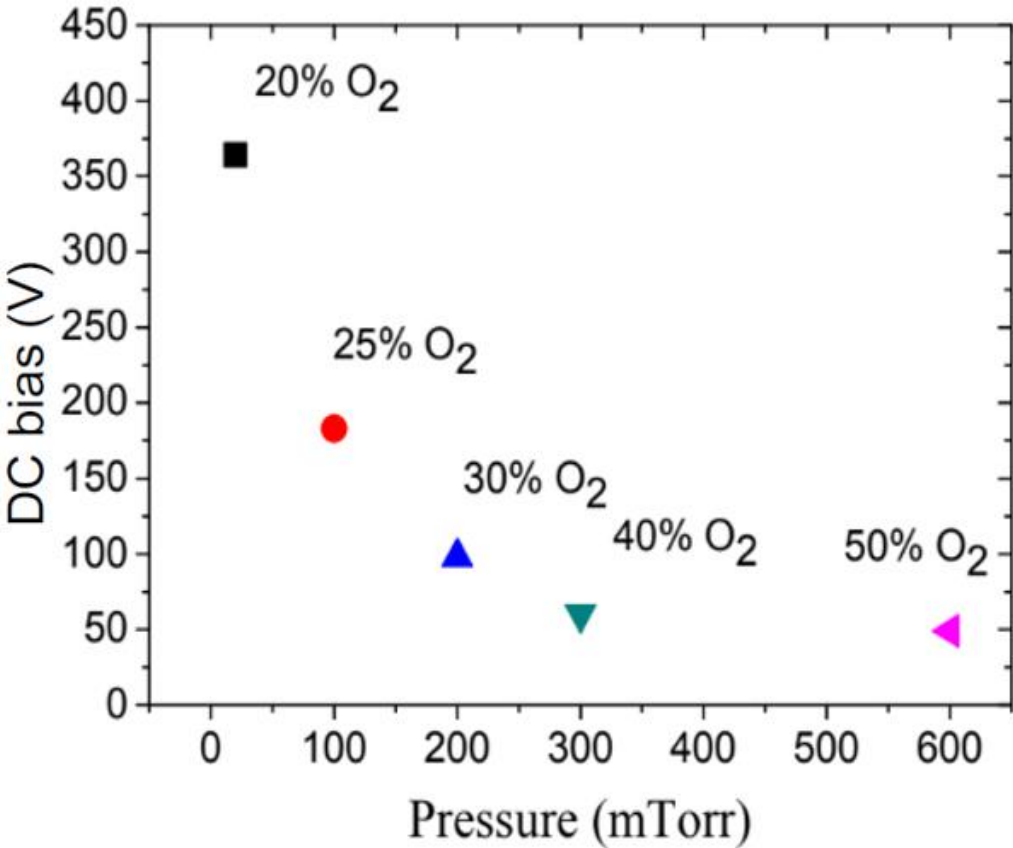


Figure 5.3: DC bias vs pressure for different %O<sub>2</sub> for peak etch rate

Using equation 4.1, we calculated the  $f_i(E)$  for different values of DC bias and the results are plotted in figure 5.4. The  $f_i(E)$  obtained is bimodal in nature, where the two peaks correspond to the maximum and minimum sheath drops where the

voltage varies slowly. We found that the peak corresponding to the maximum energy shifts toward the lower energy with increase in pressure; in other words, the broadness of the ion energy distribution  $f_i(E)$  decreases with pressure. However, the ion population corresponding to the maximum energy peak increases with pressure.

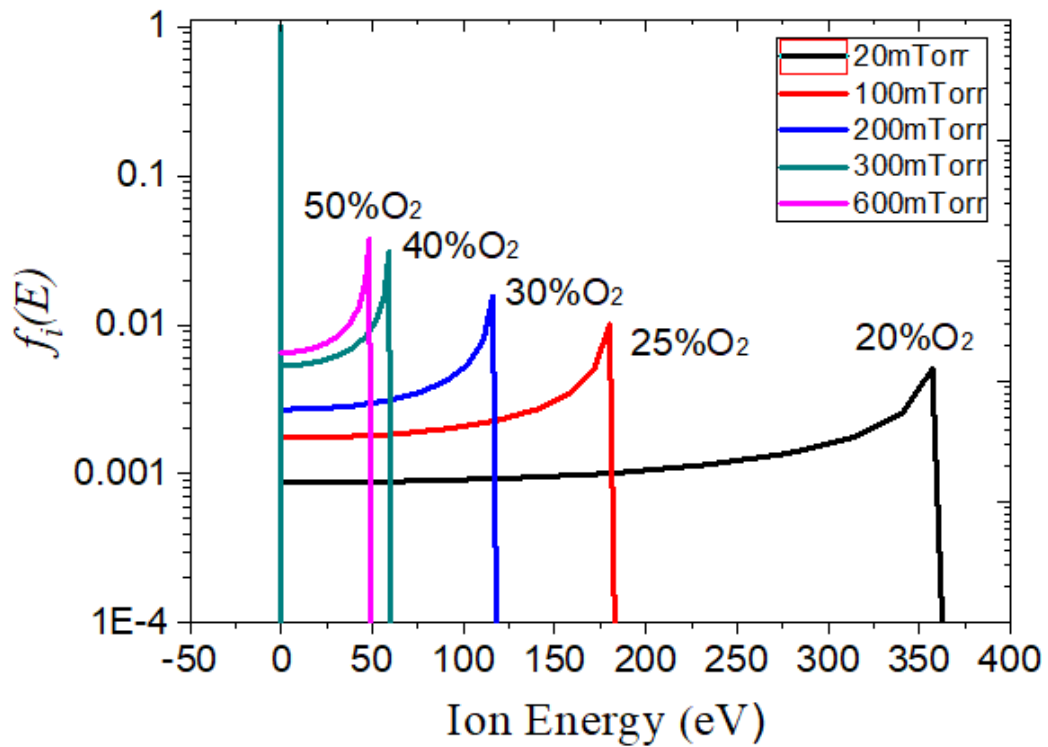


Figure 5.4:  $f_i(E)$  vs energy for different pressure and %O<sub>2</sub>

## 5.2 Experimental results and discussion

All experiments presented in this chapter are performed in OIP 100. The experimental setup is given in figure 2.2. Optical emission spectroscopy was used

to measure the density of the F atom from the intensities of the 703 nm and 750 nm lines [36]. In figure 5.5, the relative intensities of the F atom ( $I_F/I_{Ar}$ ) are shown as a function of %O<sub>2</sub>. Initially, the fluorine intensities increase with O<sub>2</sub>% and then fall down with further incrementing of the O<sub>2</sub>% in the plasma. This feature is the same for all sets of pressure. However, the peak intensities are different for different pressures. This experiment has been repeated two times to confirm the levels of fluorine and electron densities in the plasma as function of pressure and oxygen concentration.

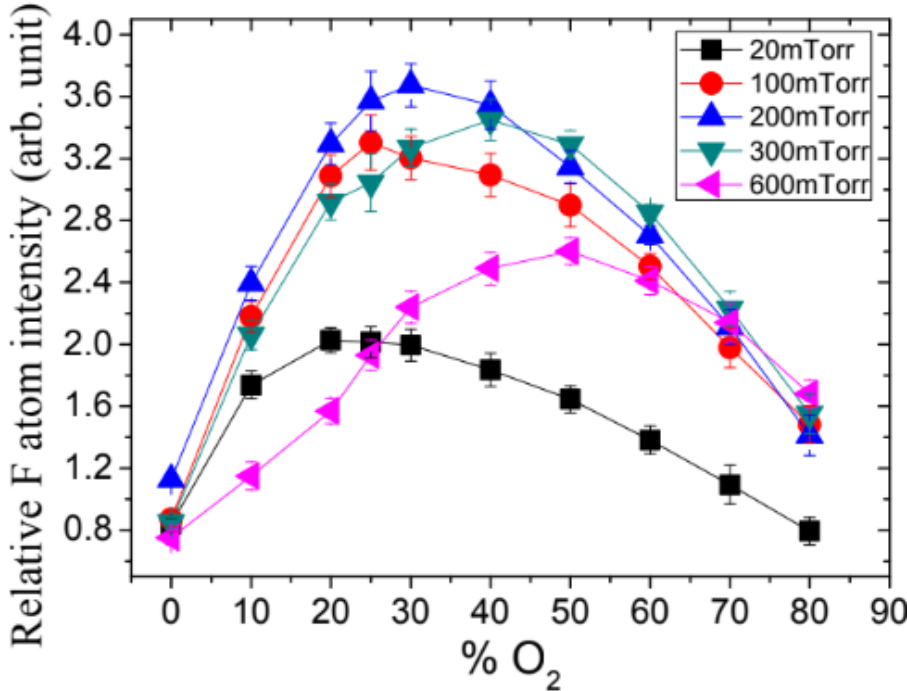


Figure 5.5: Relative intensity of the F atom as a function of %O<sub>2</sub> in SF<sub>6</sub>-O<sub>2</sub>

The density of the F atom was related to the intensities of the atomic emission lines of F and Ar as described by Alshaltami *et al.* [56]. The estimated density of the F atom can be expressed as:

$$n_F \approx 0.47 \frac{I_F}{I_{Ar}} n_{Ar} \quad (5.1)$$

where  $n_{Ar}$  is the known density of argon and  $I_F/I_{Ar}$  is the ratio of the corresponding intensities of the F atom (703 nm) to that of the Ar atom (750 nm). The densities of fluorine are plotted in figure 5.6 which shows the same trends as the F intensities.

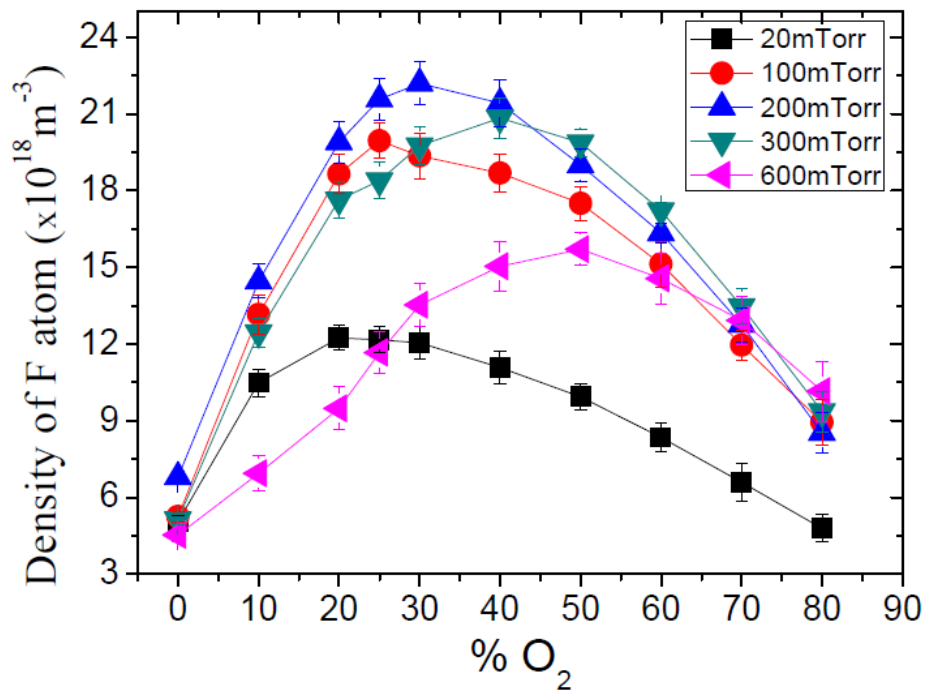


Figure 5.6: Values of fluorine densities as a function of %O<sub>2</sub> at different pressures

The density of the F and O atom as a function of power for different sets of O<sub>2</sub>% is shown in figure 5.7 and figure 5.8 respectively. We found that both F and O density increases with the applied power. An experiment is carried out in plasma chamber OIP 100 with single testing of fluorine and oxygen densities in the plasma as a function of RF power.

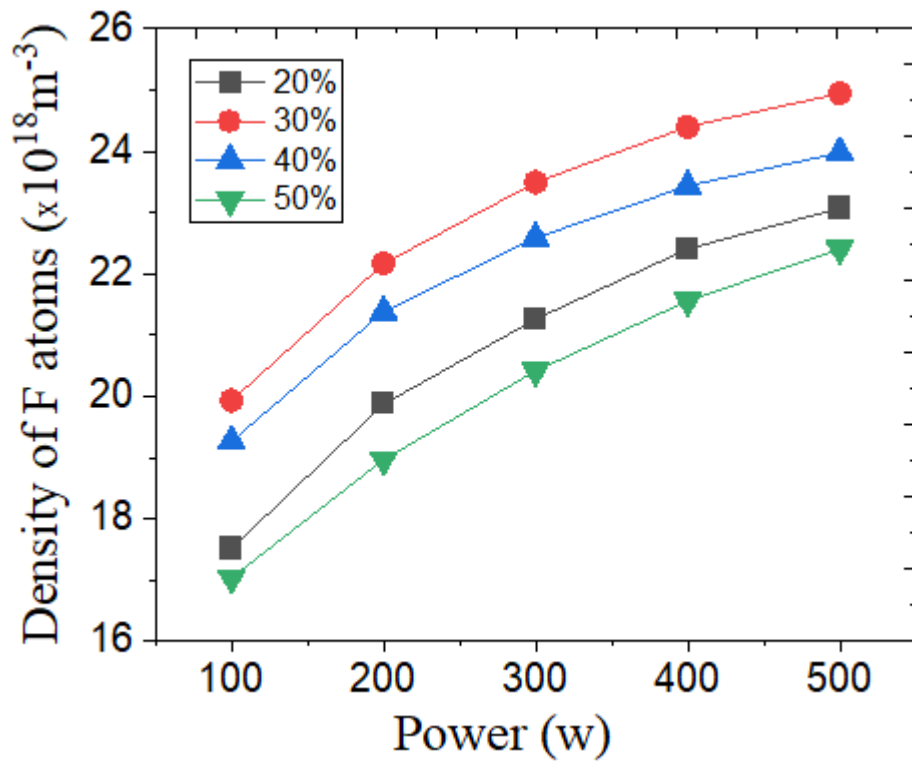


Figure 5.7: The density of F atoms as a function of power at different O<sub>2</sub> concentrations in 200 mTorr

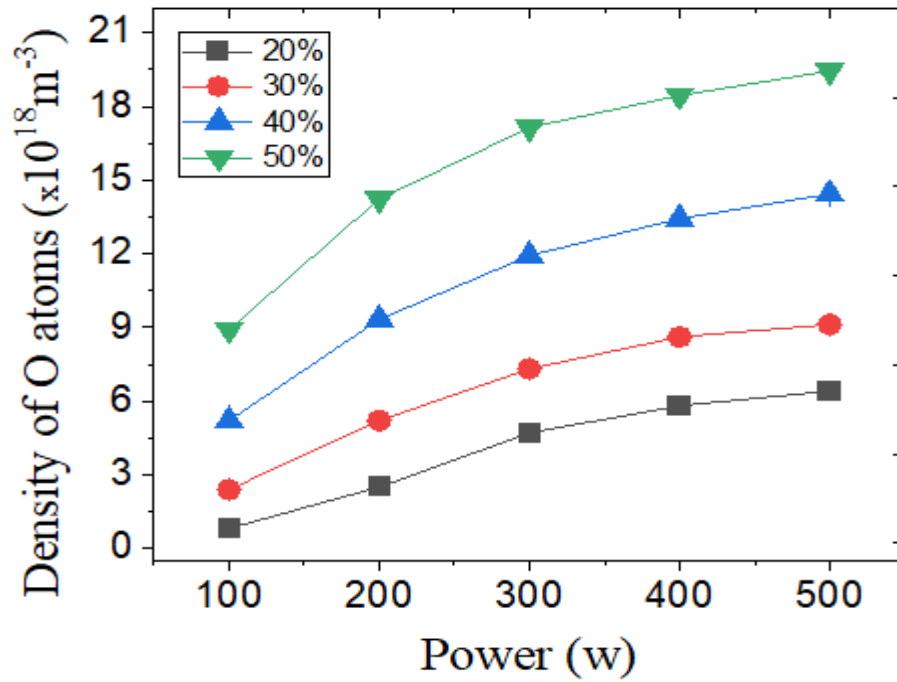


Figure 5.8: The density of O atoms as a function of power at different O<sub>2</sub> concentration and 200 mTorr

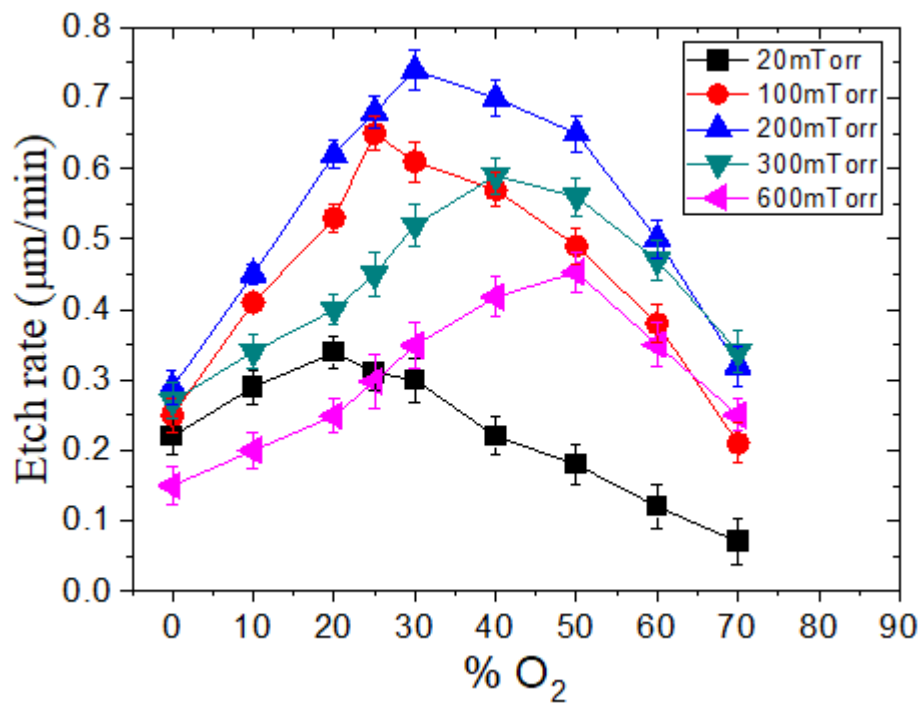


Figure 5.9: Etch rate as a function of %O<sub>2</sub> for different pressures

Figure 5.9 shows the etch rate as a function of oxygen concentration for different pressures. The etch rate was found to vary parabolically for different pressures. For instance, the etch rate is maximum at 20% O<sub>2</sub> level when the pressure is 20 mTorr. Further, the peak etch rate occurs at higher oxygen concentrations on further increase in the pressure to 600 mTorr. This is due to the fact that addition of oxygen increases the conversion of SF<sub>6</sub> by reacting with fluorosulphur radicals (refer table 3.1: Production of F from O<sub>2</sub>) and thus prevent their recombination with fluorine to reform SF<sub>6</sub>. This leads to a net increase in the F concentration. However, at higher oxygen level, i.e., above 20% for the 20 mTorr case, oxygen becomes more dominant over fluorine and, therefore, SF<sub>5</sub> recombines with F to form SF<sub>6</sub> (refer table 3.1: Destruction of F). The lower pressure in the plasma results in a longer mean free path, thus limiting the collisions, whereas higher pressure results in a shorter mean free path, which promotes the collisions in the plasma. At higher pressures, the level of SF<sub>5</sub> density increases, and to compensate, the oxygen level has to be increased to achieve the desired etch profile. Therefore, the peak etch rate occurs at higher O<sub>2</sub> levels for high pressures. This experiment has been repeated two times to confirm the levels of etch rate and etch profile in the plasma as a function of pressure and oxygen concentration.

Morshed *et al.* experimentally investigated that electron density increases with applied power and is correlated to the concentration of fluorine [53], [63]. The increase in power increases the electron density and hence increases the F density due to the electron collision with the SF<sub>6</sub> gas. This will result in a decrease in the

lateral depth. However, we also expect a degradation of photo resist due to increase in power which produces hydrogen gas. This is the only source of hydrogen in the chamber, as we are not using any gas producing hydrogen.

On the other side, oxygen concentration increases with applied power. The increase in oxygen concentration execute the oxidation of Si to SiO<sub>2</sub> (refer table 3.1: Surface oxidation). Therefore, the balanced mixture of O<sub>2</sub> and SF<sub>6</sub> is required to achieve the vertical sidewall etching. This balanced mixture may depend on various factors such as power, pressure, DC bias and O<sub>2</sub> concentration for optimum vertical sidewall etching.

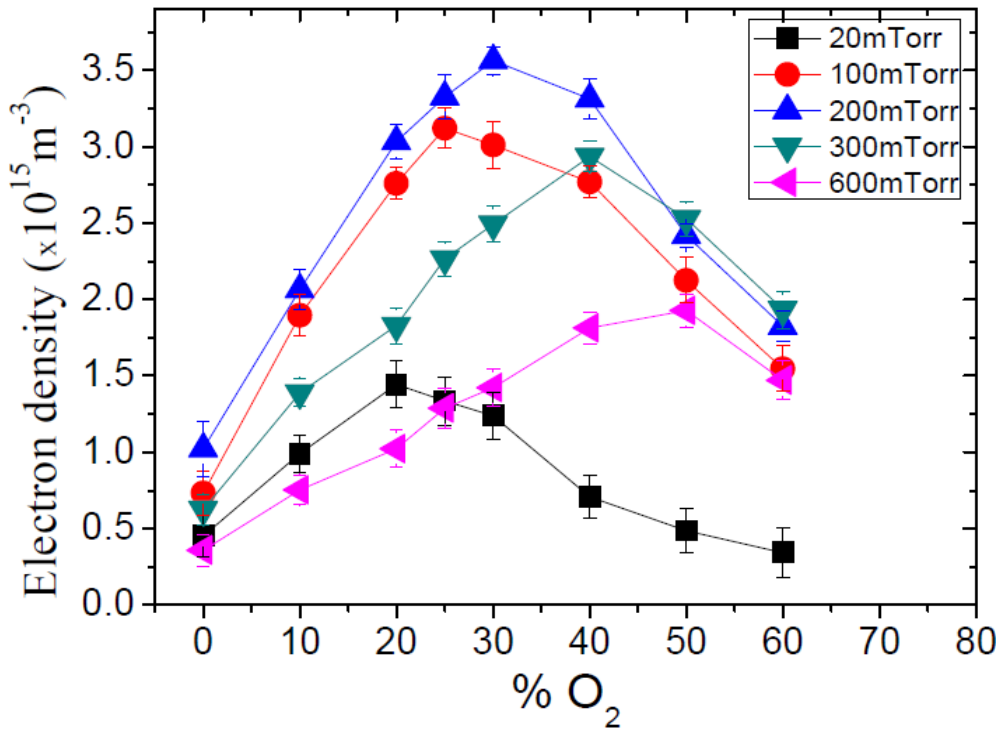


Figure 5.10: Electron density as a function of the fraction of O<sub>2</sub> corresponding to the pressure values observed in the SF<sub>6</sub>-O<sub>2</sub> plasma system

Figure 5.10 shows the electron density versus oxygen level for different pressures. The peak value of  $n_e$  is obtained at 20 mTorr and 20% O<sub>2</sub>. We found that the maximum electron density shifted to a higher O<sub>2</sub> concentration with increasing pressure. This result is in good agreement with the F density and etch rates.

We collected all the **peak etch rate points** from figure 5.9 and plotted them in figure 5.11 as a function of pressure. We found that the amount of etch rate is highest for the conditions when pressure is 200 mTorr and 30% O<sub>2</sub> level. This is because at pressures above 200 mTorr, there will be significant electron-neutral collisions in the plasma, which will reduce the density and thermal energy of F and O to perform the required etch process [64], [65].

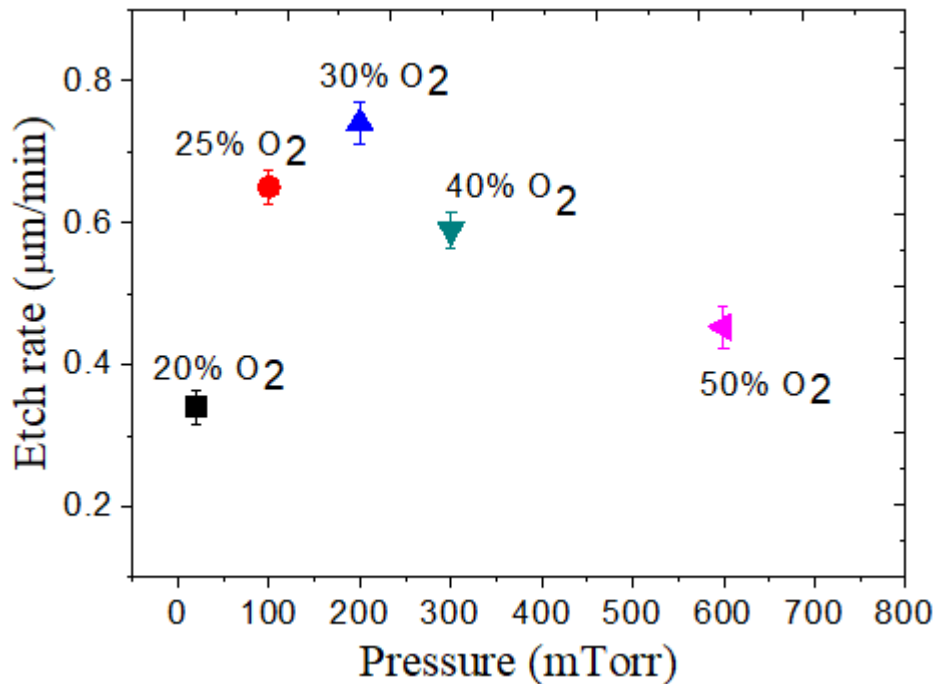


Figure 5.11: Peak of the etch rate as a function of pressures for different oxygen concentrations

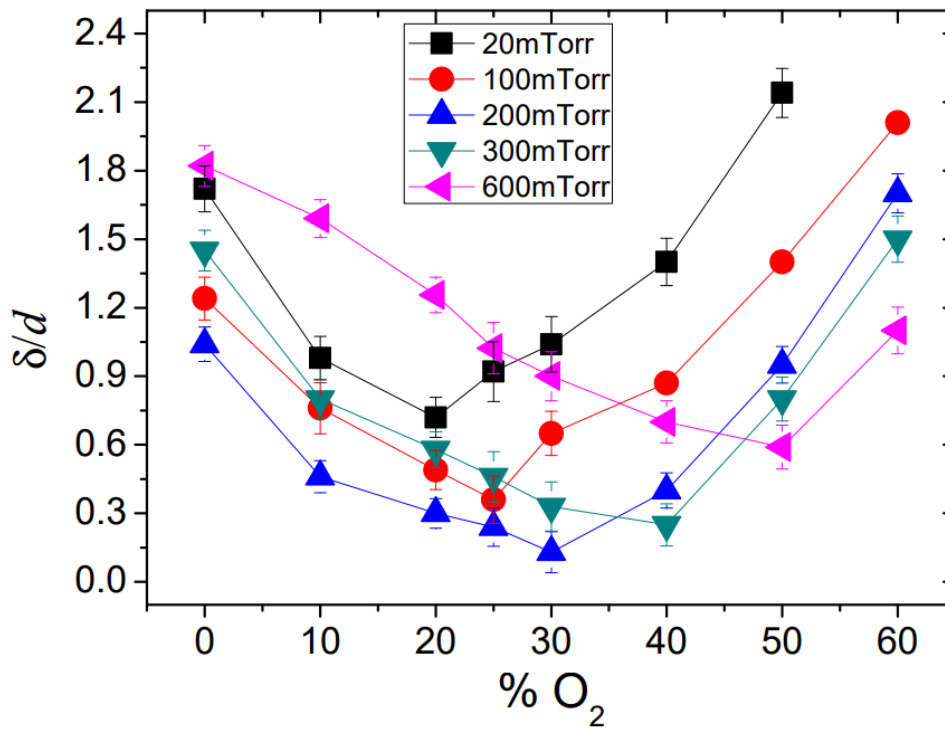


Figure 5.12: Values of  $\delta/d$  for each profile as a function of the fraction of oxygen in  $\text{SF}_6\text{-O}_2$  discharge

Figure 5.12 shows the lateral depth versus oxygen concentration at different pressures. For the peak etch rate, the lateral depth should be the minimum to achieve an anisotropic etch profile. For instance, 20%  $\text{O}_2$  results in a maximum etch rate at 20 mTorr, and the minimum lateral depth obtained under the same plasma conditions is as shown in figure 5.12. This result is consistent for all different sets of operating pressures.

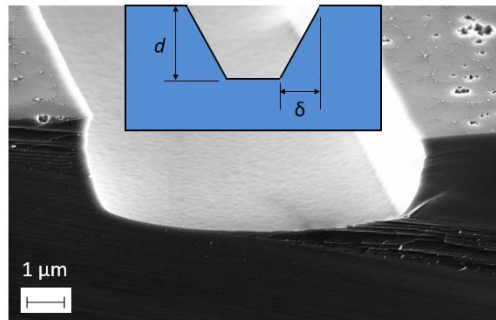


Figure 5.13. Etch profile obtained at 100 mTorr and 25% oxygen concentration, where ( $d$ ) is the depth and ( $\delta$ ) is the lateral depth.

Figure 5.13 shows the anisotropic etch profile obtained at 100 mTorr and 25% oxygen concentration. The ratio  $\delta/d$  for different plasma conditions are plotted in Fig. 5.12.

After certain level of  $O_2$  (for example:  $O_2$  – 20 % at 20mTorr), F concentration decreases with further increase in  $O_2$  concentration, as shown in figure 5.6. One of the mechanisms is that  $SF_5$  recombines with F to form  $SF_6$  due to the dilution effect causing reduction in F concentration. Another reason for the reduction of F could be due to the resonance enhanced quenching of the Argon transition 750 nm which is correlated to the electron density. Morshed *et al.* [53] found that the electron density decreases with increased  $O_2$  dissociation rate (above  $O_2=30\%$ ) in the plasma. Argon provides stability and enhances anisotropic etching and it decreases with decrease in the electron density in the plasma. Therefore, this will lead to the reduction of fluorine in the discharge.

The third possible factor for reduction in the F could be the ion energy. The ion energy is inversely related to the mass. Therefore, oxygen energy in the oxygen rich plasma would be more dominant than the F due to its lighter mass. Due to that, the plasma becomes more electronegative and we know that electron density decreases with increase in electronegativity in the plasma.

We collected the data points from the high-energy peaks from figure 5.4 and plotted in figure 5.14 as ion population (*IP*) versus energy for optimum O<sub>2</sub>% and pressure. The result shows the nonlinear trend between the population and energy, confirming the inverse correlation between the two parameters. We performed the nonlinear curve fitting method and obtained an equation, as given below:

$$IP = 0.004 + \frac{1}{2} \left( \frac{0.08}{(1+0.007E)^{3.1}} \right) \quad (5.2)$$

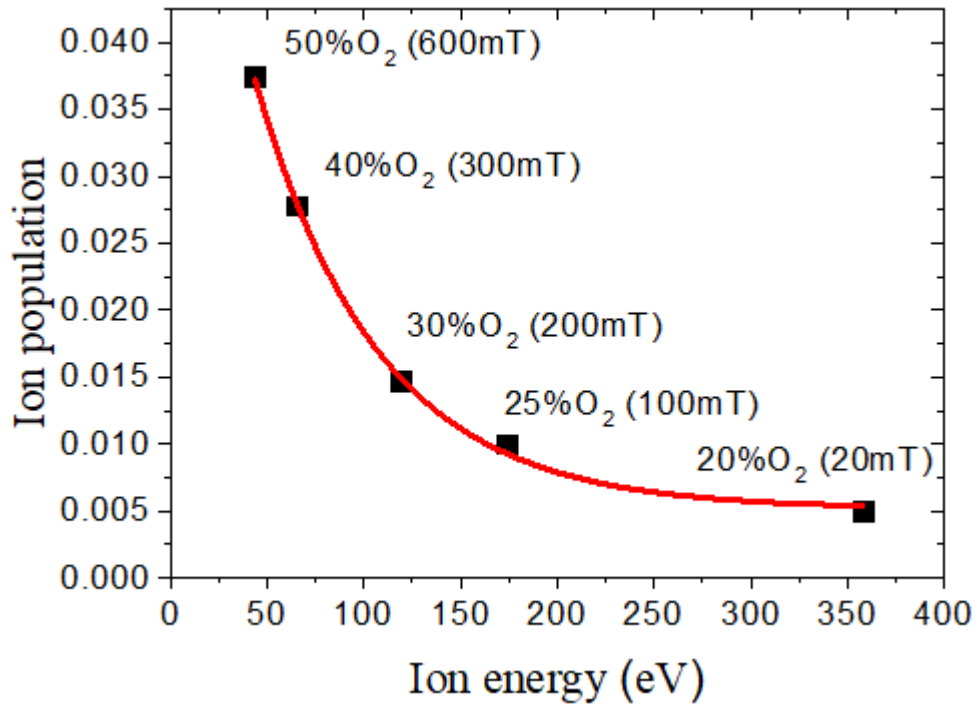


Figure 5.14: Ion population vs ion energy

This equation and the graph provided in figure 5.14 provide information about the selective etching process i.e., the pressure and O<sub>2</sub>% level required to achieve a peak etch rate for a given ion energy.

The plasma density is a function of pressure and O<sub>2</sub>%, as shown in figure 5.6. Hence, the sheath thickness will also vary with pressure and O<sub>2</sub>% in the plasma. Similarly, sheath voltage is a function of DC bias and DC bias changes with pressure and O<sub>2</sub>%, as shown in figure 5.1 and figure 5.2

The sheath thickness around the substrate electrode is given by Liebermann [62].

$$S = \frac{\sqrt{2}}{3} \left( \frac{\epsilon_0}{en_s} \right)^{1/2} \left( \frac{2V_s}{T_e V} \right)^{3/4} \quad (5.4)$$

where  $V_s$  is voltage across the sheath,  $e$  is electron charge,  $\epsilon_0$  is vacuum permittivity,  $T_e$  is electron temperature and  $n_s$  is the sheath density =  $0.61n_p$ . The above equation can be simplified further as follows:

$$S = 7544 \frac{V_s^{3/4}}{n_p^{1/2} T_e^{1/4} V} \quad (5.5)$$

It is clear from the above equation that sheath thickness is a function of plasma density, electron temperature and sheath voltage. For a given plasma density ( $10^{19} \text{ m}^{-3}$ ) and electron temperature (2 eV), the sheath thickness varies as a function of DC bias.

In accordance with our results, we found that as we increase the pressure for a given power and  $\text{O}_2\%$ , DC bias decreases and plasma density increases up to certain value, therefore the sheath thickness should decrease with the pressure as per equation 5.5, provided electron temperature is more or less constant.

In the second case, an increase in the  $\text{O}_2\%$  results in a decrease in the optimum level plasma density and an increase in the DC bias, therefore the sheath thickness increases with  $\text{O}_2\%$ . Hence, we can conclude that the sheath thickness varies with the  $\text{O}_2\%$  and pressure and we need a definite thickness or voltage across the sheath in order achieve the peak etch rate in the system. This optimum condition has been

achieved experimentally in our work and correlated with the analytical model of Ion energy distribution,  $f_i(E)$ .

### **5.3 Summary**

A detailed experimental investigation of the etch rate and etch profile is performed in SF<sub>6</sub>-O<sub>2</sub> plasma (OIP 100) by varying parameters such as pressure, oxygen concentration and DC bias voltage. We found that the peak etch rate condition discussed in chapter 3 is now strongly dependent on the operating pressure, DC bias and O<sub>2</sub> percentage. For instance, pressure of 20 mTorr, DC bias of 370 V and O<sub>2</sub> concentration of 20% gives the peak etch rate in the plasma. However, an increase in one parameter, such as pressure, can affect the whole etch process, giving rise to a peak etch rate at a higher O<sub>2</sub> percentage. The increase in pressure has a direct impact on the F and O concentrations and hence changes the conditions for the optimal etch rate. The experimental investigation of etch rates supported by the theoretical investigation of IED suggests a strong correlation between the optimal etch conditions and pressure.

# Chapter 6

## Summary, conclusions and recommendations for future research

### 6.1 Summary and conclusions

The major problem associated with the processing of silicon wafers is that the wafers are to be processed in different chambers, which is readily available rather than waiting for the right chamber. However, there is a cost associated with this protocol and it causes time delays. One of the solutions is to carry out chamber matching by making sure that the performance and output data of the chamber in use match with the reference chambers. This can only be achieved by investigating various operating parameters, such as concentration of Oxygen and Fluorine, pressure, power, and their impact on the etching process.

In this PhD work, we examine the impact of varying the important parameters on the etching process in  $\text{SF}_6\text{-O}_2$  plasma, as highlighted in the previous research carried out by various authors including our research group at Dublin City

University [Section 1.6]. These parameters include concentrations of oxygen/fluorine, pressure, power, DC bias, and SF<sub>6</sub>-O<sub>2</sub> mixture ratio. One of the most important part of our study is to compare the performance, and output of the two geometrically different Capacitively Coupled Plasma (CCP) chambers (OIP100 and OIP80+).

Silicon wafers were used to investigate the anisotropic nature of the etch profiles. The oxygen and fluorine concentrations were measured via optical emission spectroscopy using the actinometry technique, which requires the electron energy distribution function to remain unchanged under the different plasma conditions employed in this work. A Langmuir probe was used to investigate the electron energy distribution function where the chamber pressure, power and process duration were kept constant, and the oxygen concentration was varied from 0 to 60%. Scanning electron microscopy is used to show the etch profile in both chambers. We measured etch depth ( $d$ ) and lateral depth ( $\delta$ ) to estimate the etch rate ( $d/\text{time}$ ) and  $\delta/d$ .

**Summary of results:**

- In both chambers, the atomic concentrations of fluorine increase with increase in oxygen until O<sub>2</sub>=20% at 10mT and 200W.
- The concentration of Fluorine reaches its peak value at O<sub>2</sub>=20% and then decreases when O<sub>2</sub> > 20% under the same 10mT and 200W condition.

- The geometry of the chamber has a significant impact on the densities and hence on the etch rate and etch profile.
- The etch rate and densities values are higher for the smaller chamber, OIP 80+
- Any variation in the operating pressure plays an important role in changing the peak value of the density/etch rate in the plasma. For example, we obtained peak etch rate at 10mT when O<sub>2</sub>=20% and at 300mT when O<sub>2</sub>=40%.
- Both plasma systems registered the same trends of  $\delta/d$  when varied the O<sub>2</sub> concentrations in the plasma. However, the value of  $\delta/d$  at O<sub>2</sub>=20% in the case of OIP 100 is 2.5 times higher compared to OIP 80+. For optimum anisotropic etch profile,  $\delta/d \sim 0$ .
- A qualitative theoretical analysis of the ion energy distribution and its correlation with the etch rate and the density of F in SF<sub>6</sub>-O<sub>2</sub> plasma is also presented. The sheath thickness varies with the O<sub>2</sub>% and pressure and we need a definite thickness or voltage across the sheath in order to achieve the peak etch rate. This optimum condition has been achieved experimentally in our work and correlated with the analytical model of Ion energy distribution.

At lower O<sub>2</sub> concentrations (O<sub>2</sub><20%), oxygen increases the production of fluorine through the conversion of SF<sub>6</sub> by reacting with fluorosulphur radicals through SF<sub>6</sub> → SF<sub>5</sub> + F and SF<sub>5</sub> + O → SOF<sub>4</sub> + F and prevent their recombination

with fluorine to form SF<sub>6</sub> again. This results in an increase in the etch rate in the plasma. At certain O<sub>2</sub>%, F and O are nearly equally dominant and prevent further increases of the etch rate. In this condition, SF<sub>5</sub> is fully consumed in the plasma and hence the etch rate attains its peak value. Further increases in O<sub>2</sub>% in the plasma makes oxygen more dominant over fluorine and results in passivation rather than etching. This is due to the recombination of F with SF<sub>5</sub> to form SF<sub>6</sub>. As a result, the etch rate starts decreasing [7], [16]. The etch rate could also decrease due to the polymerisation of silicon where polymerization occurs when Fluorine-contained neutral species (such as SF<sub>6</sub>, SF<sub>5</sub>) and reactive radicals (such as F) will react with the silica to form volatile products and when react with O form siliconoxyfluoride SiO<sub>x</sub>F<sub>y</sub> layer. The polymerisation process prevents F from interacting with the silicon surface and result in decrease in the etch rate as well.

The etch rate values are higher for the smaller chamber, OIP 80+, because it holds more energetic particles, resulting in increasing effective collisions, and hence densities. Another aspect of our work covers how oxygen concentration and operating pressure changes the conditions to achieve optimal etch rates and profile. For example, the etch rate is at maximum at O<sub>2</sub>=20% when plasma operates at low pressure, like 10 mTorr and an RF power of 200 W. This peak etch rate shifts to O<sub>2</sub> = 40% when the operating pressure is 300 mTorr. This is because the fluorine densities increase with pressure. Therefore, more oxygen will be needed to compensate for the effect of F for plasma etching. The electron and ion densities are in good agreement with the results obtained for the etch rates.

The etch rate could also decrease due to the polymerisation of silicon, especially on the etched trenches and sidewalls. The polymerisation process prevents F from interacting with the silicon surface and result in decrease in the etch rate as well. The second possibility is that F density can increase while etch rate decreases due to the chemisorption of O atoms on the  $\text{SF}_6$  and hence it forms an oxide-like layer resulting in reduction in the etch rate. On the other hand, F density continuously increases in this case.

The ion energy distribution in RF plasma and its broadening are found to be related to the optimal etch conditions. However, these experimental results are limited to a condition of constant power of 200W. The full performance of the chambers should be compared by investigating the power required to maintain the same amount of density in the plasma. This may conclude that the chamber geometry plays an important role in changing the densities of F and O atoms in a plasma, and to choose a chamber that produce a required amount of species to achieve optimal etch conditions.

Both chambers exhibit the same trend of etch rate. However, the etch rate in the case of OIP 80+ is around 2.5 times higher compared to the case of OIP 100 because of the different chamber volume. The smaller the volume, the greater will be the energy supplied to the individual particles to cause more effective collisions. Therefore, density increases for the smaller chambers such as OIP 80+ as compared to the OIP 100.

The difference in the etch rate and etch profile for the two different plasma chambers accounts for their differences in geometry. OIP 80+ (1.2) has a smaller ratio of electrode sizes (grounded/power) compared to OIP 100 (1.5). The ratio of electrode sizes can significantly affect the ion energy. This is because self-bias is higher for smaller ratio, and that means more energetic ions can be created in the plasma. The smaller the ratio of the electrode sizes, the greater is the ion bombardment. That is why the etch rate of OIP 80+ is greater than that of the OIP 100.

This research findings can be used to further improve the de novo method of chamber matching, where the quality etch results can be obtained by controlling the O<sub>2</sub> concentration, pressure, and power. These parameters have direct impact on the etch rates and etch profiles. We have demonstrated that how one can select a key input parameter that can tune the etching conditions without any extra cost of manufacturing.

## **6.2 Recommendations for future research**

Ion energy plays an important role in achieving the desired profile. This is because the sheath adjacent to the substrate affected the ion flux and ion energy and impacted the surface. The selective etching process is critical in case of high ion energy plasma. This means that the selective etching process including the etch profile may work under certain operating conditions. However, the sheath thickness is the main parameter which can alter the path of the ions approaching

the substrate and that can result in uniformity in the etching. The sheath thickness depends on the sheath electric field and the ion mean free path, which can be controlled by varying the amplitude of the RF voltage or by changing the DC bias at the substrate electrode. Using these operating parameters, we can optimise the ion energy at the substrate, and hence the etching profile.

*What is the next step in future research work?*

1. Measurement of ion energy distribution near the substrate to get a better insight into the etch process.

The increase of ion flux involved in the etching process affects both the etch rate and etch quality, but in a contrary way. We can achieve a better etch rate simply through attaining a higher ion flux. However, this could also mean a higher significant increase in the surface roughness. Thus, a detailed investigation of the ion flux and its influence on the plasma etch process is needed. The ion energy distribution can be measured by using the retarding field analyser (RFA).

2. Measurement of sheath thickness to understand how operating parameters like pressure and power change the etch rate and profile.

## References

- [1] W. Crookes, ‘On a fourth state of matter’, *Proceedings of the Royal Society of London*, vol. 30, no. 200–205, pp. 469–472, 1879.
- [2] S. Samukawa *et al.*, ‘The 2012 plasma roadmap’, *J.Phys.D*, vol. 45, no. 25, p. 253001, 2012.
- [3] R. J. Shul and S. J. Pearton, *Handbook of advanced plasma processing techniques*. Springer Science & Business Media, 2011.
- [4] K. Wiesemann, ‘A short introduction to plasma physics’, *arXiv preprint arXiv:1404.0509*, 2014.
- [5] P. Yang, R. Yan, and M. Fardy, ‘Semiconductor nanowire: what’s next?’, *Nano letters*, vol. 10, no. 5, pp. 1529–1536, 2010.
- [6] D. L. Flamm, ‘Mechanisms of silicon etching in fluorine-and chlorine-containing plasmas’, *Pure and Applied Chemistry*, vol. 62, no. 9, pp. 1709–1720, 1990.
- [7] D. M. Manos and D. L. Flamm, *Plasma etching: an introduction*. Elsevier, 1989.
- [8] H. F. Winters, ‘The role of chemisorption in plasma etching’, *J.Appl.Phys.*, vol. 49, no. 10, pp. 5165–5170, 2008.
- [9] A. K. Paul, A. K. Dimri, and S. Mohan, ‘Fabrication of micromechanical structures in silicon using SF<sub>6</sub>/O<sub>2</sub> gas mixtures’, 1999, pp. 2–8.

- [10] H. Park, C. Garvin, D. Grimard, and J. Grizzle, 'Control of ion energy in a capacitively coupled reactive ion etcher', *J.Electrochem.Soc.*, vol. 145, no. 12, pp. 4247–4252, 1998.
- [11] M. Tichý *et al.*, 'Langmuir probe diagnostics of a plasma jet system', *Plasma Sources Sci.Technol.*, vol. 18, no. 1, p. 014009, 2008.
- [12] J. Marino, F. Rossi, M. Ouladsine, and J. Pinaton, 'Unsupervised Semiconductor chamber matching based on shape comparison', *IFAC-PapersOnLine*, vol. 50, no. 1, pp. 3905–3910, 2017.
- [13] T.-H. Pan, D. S.-H. Wong, and S.-S. Jang, 'Chamber matching of semiconductor manufacturing process using statistical analysis', *IEEE Transactions on Systems, Man, and Cybernetics, Part C (Applications and Reviews)*, vol. 42, no. 4, pp. 571–576, 2011.
- [14] R. d'Agostino and D. L. Flamm, 'Plasma etching of Si and SiO<sub>2</sub> in SF<sub>6</sub>-O<sub>2</sub> mixtures', *J.Appl.Phys.*, vol. 52, no. 1, pp. 162–167, 1981.
- [15] S. Tachi, K. Tsujimoto, and S. Okudaira, 'Low-temperature reactive ion etching and microwave plasma etching of silicon', *Appl.Phys.Lett.*, vol. 52, no. 8, pp. 616–618, 1988.
- [16] R. Legtenberg, H. Jansen, M. de Boer, and M. Elwenspoek, 'Anisotropic reactive ion etching of silicon using SF<sub>6</sub>/O<sub>2</sub>/CHF<sub>3</sub> gas mixtures', *J.Electrochem.Soc.*, vol. 142, no. 6, pp. 2020–2028, 1995.
- [17] H. Jansen, M. Boer, J. Burger, R. Legtenberg, and M. Elwenspoek, 'The black silicon method II: The effect of mask material and loading on the reactive ion etching of deep silicon trenches', *Microelectronic engineering*, vol. 27, no. 1–4, pp. 475–480, 1995.

- [18] K. Nojiri, K. Tsunokuni, and K. Yamazaki, 'High rate and highly selective anisotropic etching for WSi x/poly-Si using electron cyclotron resonance plasma', *Journal of Vacuum Science & Technology B: Microelectronics and Nanometer Structures Processing, Measurement, and Phenomena*, vol. 14, no. 3, pp. 1791–1795, 1996.
- [19] H. Jansen, H. Gardeniers, M. de Boer, M. Elwenspoek, and J. Fluitman, 'A survey on the reactive ion etching of silicon in microtechnology', *J Micromech Microengineering*, vol. 6, no. 1, p. 14, 1996.
- [20] R. Mansano, P. Verdonck, H. Maciel, and M. Massia, 'Anisotropic inductively coupled plasma etching of silicon with pure SF<sub>6</sub>', *Thin Solid Films*, vol. 343, pp. 378–380, 1999.
- [21] V. Yunkin, D. Fischer, and E. Voges, 'Highly anisotropic selective reactive ion etching of deep trenches in silicon', *Microelectronic Engineering*, vol. 23, no. 1–4, pp. 373–376, 1994.
- [22] W. Chen and B. Abraham-Shrauner, 'The effects of ion sheath collisions on trench etch profiles', *J.Appl.Phys.*, vol. 81, no. 6, pp. 2547–2554, 1997.
- [23] S. Gomez, R. Jun Belen, M. Kiehlbauch, and E. S. Aydil, 'Etching of high aspect ratio structures in Si using SF<sub>6</sub>/O<sub>2</sub> plasma', *Journal of Vacuum Science & Technology A: Vacuum, Surfaces, and Films*, vol. 22, no. 3, pp. 606–615, 2004.
- [24] J. M. Stillahn, J. Zhang, and E. R. Fisher, 'Surface interactions of SO<sub>2</sub> and passivation chemistry during etching of Si and SiO<sub>2</sub> in SF<sub>6</sub>/O<sub>2</sub> plasmas', *Journal of Vacuum Science & Technology A: Vacuum, Surfaces, and Films*, vol. 29, no. 1, p. 011014, 2011.

- [25] H. Zou, 'Anisotropic Si deep beam etching with profile control using SF<sub>6</sub>/O<sub>2</sub> Plasma', *Microsystem technologies*, vol. 10, no. 8–9, pp. 603–607, 2004.
- [26] Y.-D. Lim, S.-H. Lee, W. J. Yoo, O.-J. Jung, S.-C. Kim, and H.-C. Lee, 'Roles of F and O radicals and positive ions in a SF<sub>6</sub>/O<sub>2</sub> plasma in forming deep via structures', *Journal of Korean Physical Society*, vol. 54, p. 1774, 2009.
- [27] M. Morshed and S. Daniels, 'Electron Density and Optical Emission Measurements of SF<sub>6</sub>/O<sub>2</sub> Plasmas for Silicon Etch Processes', *Plasma Science and Technology*, vol. 14, no. 4, p. 316, 2012.
- [28] V. M. Donnelly and A. Kornblit, 'Plasma etching: Yesterday, today, and tomorrow', *Journal of Vacuum Science & Technology A: Vacuum, Surfaces, and Films*, vol. 31, no. 5, p. 050825, 2013.
- [29] B.-S. Kim, J. S. Kim, Y. M. Park, B.-Y. Choi, and J. Lee, 'Mg ion implantation on SLA-treated titanium surface and its effects on the behavior of mesenchymal stem cell', *Materials Science and Engineering: C*, vol. 33, no. 3, pp. 1554–1560, 2013.
- [30] P. Pankajakshan, S. Sanyal, O. E. de Noord, I. Bhattacharya, A. Bhattacharyya, and U. Waghmare, 'Machine learning and statistical analysis for materials science: stability and transferability of fingerprint descriptors and chemical insights', *Chemistry of Materials*, vol. 29, no. 10, pp. 4190–4201, 2017.
- [31] E. P. Stuckert, C. J. Miller, and E. R. Fisher, 'The effect of Ar/O<sub>2</sub> and H<sub>2</sub>O plasma treatment of SnO<sub>2</sub> nanoparticles and nanowires on carbon monoxide and benzene detection', *ACS Applied Materials & Interfaces*, vol. 9, no. 18, pp. 15733–15743, 2017.

- [32] D. Yang, J. Wang, R. Li, Y. Ma, and L. Ma, 'Extremely vertical sidewall trench etching on silicon substrate and modelling etching using artificial neural network', *Materials Research Express*, vol. 6, no. 12, p. 125902, 2019.
- [33] M. Madou, *Fundamentals of microfabrication: the science of miniaturization*. CRC press, 2002.
- [34] A. N. Zaidel, V. Prokof'ev, and S. Raiskii, 'Tables of spectral lines', *New York: IFI-Plenum, 1970*, vol. 1, 1970.
- [35] A. Granier, D. Chereau, K. Henda, R. Safari, and P. Leprince, 'Validity of actinometry to monitor oxygen atom concentration in microwave discharges created by surface wave in O<sub>2</sub>-N<sub>2</sub> mixtures', *J.Appl.Phys.*, vol. 75, no. 1, pp. 104–114, 1994.
- [36] J. Coburn and M. Chen, 'Optical emission spectroscopy of reactive plasmas: A method for correlating emission intensities to reactive particle density', *J.Appl.Phys.*, vol. 51, no. 6, pp. 3134–3136, 1980.
- [37] J. Conway, S. Kechkar, C. Gaman, M. Turner, and S. Daniels, 'Use of particle-in-cell simulations to improve the actinometry technique for determination of absolute atomic oxygen density', *Plasma Sources Sci.Technol.*, vol. 22, no. 4, p. 045004, 2013.
- [38] S. Kechkar, S. Babu, P. Swift, C. Gaman, S. Daniels, and M. Turner, 'Investigation of absolute atomic fluorine density in a capacitively coupled SF<sub>6</sub>/O<sub>2</sub>/Ar and SF<sub>6</sub>/Ar discharge', *Plasma Sources Sci.Technol.*, vol. 23, no. 6, p. 065029, 2014.

- [39] C. K. Hanish, J. W. Grizzle, and F. Teny Jr, 'Estimating and controlling atomic chlorine concentration via actinometry', *Semiconductor Manufacturing, IEEE Transactions on*, vol. 12, no. 3, pp. 323–331, 1999.
- [40] A. D. Richards, B. E. Thompson, K. D. Allen, and H. H. Sawin, 'Atomic chlorine concentration measurements in a plasma etching reactor. I. A comparison of infrared absorption and optical emission actinometry', *J.Appl.Phys.*, vol. 62, no. 3, pp. 792–798, 1987.
- [41] H.-J. Tiller, D. Berg, and R. Mohr, 'Decomposition of  $\text{CCl}_4$  in an RF discharge—A gas chromatography and time-resolved emission spectroscopy study', *Plasma Chem.Plasma Process.*, vol. 1, no. 3, pp. 247–260, 1981.
- [42] J. Booth, O. Joubert, J. Pelletier, and N. Sadeghi, 'Oxygen atom actinometry reinvestigated: Comparison with absolute measurements by resonance absorption at 130 nm', *J.Appl.Phys.*, vol. 69, no. 2, pp. 618–626, 1991.
- [43] F. F. Chen and J. P. Chang, *Lecture notes on principles of plasma processing*. Springer Science & Business Media, 2012.
- [44] B. N. Chapman, 'Glow discharge processes: sputtering and plasma etching', 1980.
- [45] C. Steinbrüchel, 'A new method for analyzing Langmuir probe data and the determination of ion densities and etch yields in an etching plasma', *Journal of Vacuum Science & Technology A: Vacuum, Surfaces, and Films*, vol. 8, no. 3, pp. 1663–1667, 1990.
- [46] R. L. Merlino, 'Understanding Langmuir probe current-voltage characteristics', *American Journal of Physics*, vol. 75, no. 12, pp. 1078–1085, 2007.

- [47] M. Schabel, V. Donnelly, A. Kornblit, and W. Tai, ‘Determination of electron temperature, atomic fluorine concentration, and gas temperature in inductively coupled fluorocarbon/rare gas plasmas using optical emission spectroscopy’, *Journal of Vacuum Science & Technology A*, vol. 20, no. 2, pp. 555–563, 2002.
- [48] J.-S. Jenq, J. Ding, J. W. Taylor, and N. Hershkowitz, ‘Absolute fluorine atom concentrations in RIE and ECR CF<sub>4</sub> plasmas measured by actinometry’, *Plasma Sources Sci.Technol.*, vol. 3, no. 2, p. 154, 1994.
- [49] Y. Kawai, K. Sasaki, and K. Kadota, ‘Comparison of the fluorine atom density measured by actinometry and vacuum ultraviolet absorption spectroscopy’, *Japanese journal of applied physics*, vol. 36, no. 9A, p. L1261, 1997.
- [50] H. Katsch, A. Tewes, E. Quandt, A. Goehlich, T. Kawetzki, and H. Döbele, ‘Detection of atomic oxygen: Improvement of actinometry and comparison with laser spectroscopy’, *J.Appl.Phys.*, vol. 88, no. 11, pp. 6232–6238, 2000.
- [51] V. Gedeon, S. Gedeon, V. Lazur, E. Nagy, O. Zatsarinny, and K. Bartschat, ‘B-spline R-matrix-with-pseudostates calculations for electron-impact excitation and ionization of fluorine’, *Physical Review A*, vol. 89, no. 5, p. 052713, 2014.
- [52] R. Knizikevičius, ‘Simulations of Si and SiO<sub>2</sub> etching in SF<sub>6</sub>/O<sub>2</sub> plasma’, *Vacuum*, vol. 83, no. 6, pp. 953–957, 2009.
- [53] M. Morshed and S. Daniels, ‘Electron Density and Optical Emission Measurements of SF<sub>6</sub>/O<sub>2</sub> Plasmas for Silicon Etch Processes’, *Plasma Science and Technology*, vol. 14, no. 4, p. 316, 2012.

- [54] J. Coburn and M. Chen, 'Dependence of F atom density on pressure and flow rate in CF<sub>4</sub> glow discharges as determined by emission spectroscopy', *Journal of Vacuum Science and Technology*, vol. 18, no. 2, pp. 353–356, 1981.
- [55] N. Camara and K. Zekentes, 'Study of the reactive ion etching of 6H–SiC and 4H–SiC in SF<sub>6</sub>/Ar plasmas by optical emission spectroscopy and laser interferometry', *Solid-State Electronics*, vol. 46, no. 11, pp. 1959–1963, 2002.
- [56] K. A. Alshaltami, M. Morshed, C. Gaman, J. Conway, and S. Daniels, 'Experimental investigation of SF<sub>6</sub>–O<sub>2</sub> plasma for advancement of the anisotropic Si etch process', *Journal of Vacuum Science & Technology A: Vacuum, Surfaces, and Films*, vol. 35, no. 3, p. 031307, 2017.
- [57] R. Knizikevičius, 'Simulations of Si and SiO<sub>2</sub> etching in SF<sub>6</sub>/O<sub>2</sub> plasma', *Vacuum*, vol. 83, no. 6, pp. 953–957, 2009.
- [58] D. Gahan, B. Dolinaj, and M. Hopkins, 'Comparison of plasma parameters determined with a Langmuir probe and with a retarding field energy analyzer', *Plasma Sources Sci.Technol.*, vol. 17, no. 3, p. 035026, 2008.
- [59] E. Kawamura, V. Vahedi, M. Lieberman, and C. Birdsall, 'Ion energy distributions in rf sheaths; review, analysis and simulation', *Plasma Sources Sci.Technol.*, vol. 8, no. 3, p. R45, 1999.
- [60] D. L. Flamm, V. M. Donnelly, and J. A. Mucha, 'The reaction of fluorine atoms with silicon', *J.Appl.Phys.*, vol. 52, no. 5, pp. 3633–3639, 1981.
- [61] C. Mogab, A. Adams, and D. L. Flamm, 'Plasma etching of Si and SiO<sub>2</sub>—The effect of oxygen additions to CF<sub>4</sub> plasmas', *J.Appl.Phys.*, vol. 49, no. 7, pp. 3796–3803, 2008.

- [62] M. A. Lieberman and A. J. Lichtenberg, 'Principles of Plasma Discharges and Materials Processing, 2005', 2005.
- [63] M. M. Morshed and S. M. Daniels, 'Effect of Positive Photoresist on Silicon Etching by Reactive Ion Etching Process', *IEEE Trans. Plasma Sci.*, vol. 38, no. 6, pp. 1512–1516, 2010.
- [64] L. G. Christophorou and J. K. Olthoff, 'Electron interactions with plasma processing gases: present status and future needs', *Appl. Surf. Sci.*, vol. 192, no. 1–4, pp. 309–326, 2002.
- [65] L. G. Christophorou, *Electron—Molecule Interactions and Their Applications: Volume 2*, vol. 2. Academic Press, 2013.